An Observational Comparison of Level of Neutral Buoyancy and Level of Maximum Detrainment in Tropical Deep Convective Clouds

Dié Wang[1], Michael P. Jensen[1], Jennifer A. D'Iorio[2], Gina Jozef[3], Scott E. Giangrande[1], Karen L. Johnson[1], Zhengzhao Johnny Luo[4], Mariusz Starzec[5], Gretchen L. Mullendore[5]

[1]Department of Environmental and Climate Sciences, Brookhaven National Laboratory, Upton, NY 11973
[2]Department of Meteorology and Atmospheric Science, Pennsylvania State University, University Park, PA 16802
[3]Department of Environmental Science, Colorado College, Colorado Springs, CO 80903
[4]Department of Earth and Atmospheric Sciences, City College of New York, New York, NY 10031
[5]Department of Atmospheric Sciences, University of North Dakota, Grand Forks, ND 58202

Key Points:

- A proxy for the effective bulk entrainment for tropical deep convection is estimated based on ARM radiosonde and radar observations.
- Oceanic deep convection in the Tropics suggests enhanced effective bulk entrainment, associated with higher CAPE and more moist conditions.
- For continental events, higher pre-storm CAPE, higher RH, and stronger wind shear favor increased effective bulk entrainment.

Corresponding author: Dié Wang, diewang@bnl.gov

Abstract

Tropical deep convective clouds are important drivers of large-scale atmospheric circulation representing the main vertical transport pathway through the depth of the troposphere for heat, momentum, water, and chemical species. The strength and depth of this transport are impacted by the convective updraft size and intensity that are driven by buoyancy, dynamical forcing, and mixing of environmental air, i.e., entrainment. In this study, we identify tropical deep convective systems with well-defined forward anvils using Atmospheric Radiation Measurement (ARM) ground-based profiling radars, at three ARM fixed-sites in the Tropical Western Pacific (TWP; i.e., Manus, Nauru, Darwin) and three ARM Mobile Facility deployments in Niamey, Niger; Gan Island, Maldives; and Manacapuru, Brazil. We use the difference between the level of neutral buoyancy (LNB) and the level of maximum detrainment (LMD) as a proxy for the effective bulk convective entrainment (ε_{proxy}). The LNB, the theoretical height that a parcel raised above the level of free convection would reach with no mixing, is calculated based on pre-convection radiosonde measurements using parcel theory. The LMD is the height of the maximum reflectivity observed in forward anvil clouds by profiling radars.

Deep convective systems over the TWP show higher LNBs that extend to 16.3 km on average and larger ε_{proxy} (median LNB minus LMD up to 6.5 km) compared to their continental counterparts in the Amazon and West Africa. Oceanic conditions show larger convective available potential energy (CAPE) coupled with higher moisture at low levels which favors larger ε_{proxy}. In contrast, continental cases initiate and develop under high convective inhibition, steeper environmental lapse rate, and high wind shear conditions, which show smaller offset between LNB and LMD. Deep convective cases that promote significant cold pools at the surface experience less ε_{proxy}. Using a Random Forest regression algorithm, CAPE is associated with the highest feature importance score for predicting convective ε_{proxy}, followed by low-level relative humidity. For continental cases, the low-level wind shear also indicates higher importance.

1 Introduction

A common feature of tropical regions, deep convective clouds help regulate the global energy and water cycles (e.g., Fritsch et al., 1986; R. A. Houze, 2004; R. A. Houze Jr., 2018), and are the primary vehicle to transport heat, moisture, and momentum from the boundary layer upward to the dry upper troposphere and lower stratosphere through convective updrafts (e.g., Bretherton & Smolarkiewicz, 1989; de Rooy & Pier Siebesma, 2010). As cumulus convection deepens, an important aspect of its development is the horizontal outflow that preferentially occurs in the upper troposphere and is controlled by the strength of the convective updrafts. This outflow from the convective cores is called dynamical detrainment (e.g., Raga et al., 1990; Dawe & Austin, 2011), and these detrainment processes help form widespread stratiform and long-lasting anvil clouds that influence the net radiative forcing of the atmosphere (e.g., Hartmann et al., 2001; Jensen et al., 2002; Jensen & Del Genio, 2003; Stephens, 2005). Complementing these mass detrainment processes are cloud entrainment processes that govern the updraft size and intensity, and affect the strength and depth of this mass transport (e.g., Stommel, 1947). Moreover, entrainment cools the ascending convective parcels and decreases the liquid water content in active convection by mixing drier, cooler environmental air into moist updraft regions. Thus, entrainment processes result in a dampening of convective buoyancy and a subsequent decrease in the level of maximum detrainment (e.g., Derbyshire et al., 2004; Del Genio & Wu, 2010).

The treatment of the cloud entrainment/detrainment process has been identified as a bottleneck for current global climate model (GCM) representation of deep convection, as well as simulations to cloud-resolving model (CRM) scales (e.g., Kain & Fritsch, 1990; Bretherton et al., 2004; Romps, 2010; Klocke et al., 2011; Kim & Kang, 2012; Del Genio et al., 2012; Stirling & Stratton, 2012; Anber et al., 2019). For instance, a small change to the parameterization of the entrainment rate can introduce a significant shift in the timing or amplitude of the convective diurnal cycle (e.g., Yang & Slingo, 2001; Del Genio & Wu, 2010), thereby altering the large-scale circulation and resulting in significant climate variability (e.g., Tokioka et al., 1988; Maloney & Hartmann, 2001; Sanderson et al., 2008; Hannah & Maloney, 2011). One explanation for the continuing challenge is that observational constraints for model process improvement (or convective parameterization) including cloud entrainment rates, mass flux, and mass detrainment properties for deep and/or tropical cumulus are extremely difficult to obtain. Moreover, convective cloud

processes operate across a wide range of spatiotemporal scales, and aircraft in-situ observations are costly, unavailable over remote tropical/oceanic regions, and hazardous in the stronger convective cloud conditions (e.g., Guo et al., 2015). Thus, observational constraints are often restricted to a small subset of convective cloud-types and thermodynamic conditions for limited parameterization improvement in the models (e.g., Cohen, 2000; Mullendore et al., 2005).

This study is motivated by the deficiencies in our observational understanding of the bulk entrainment and mass detrainment processes that impact tropical deep convection. We emphasize the mass detrainment aspects of this problem, as it can be argued that current remote-sensing instrumentation are capable of characterizing the heights at which most of the air transported by convective updrafts detrains in convective anvil cloud regions. In this regard, observed detrainment levels are found to be strongly dependent on the updraft strength and the conditions in which that deep convection initiates and develops (e.g., Hartmann & Larson, 2002). Furthermore, estimates for the observed levels of maximum detrainment (as well as the net detrainment mass flux) are expected to vary significantly with convection type, size, and age (e.g., Barnes et al., 1996; Norgren et al., 2016). Previous studies (e.g., Takahashi & Luo, 2012) have argued that differences in the detrained outflow heights and the level of neutral buoyancy can act as a simple proxy for effective bulk convective entrainment. These concepts have been applied to satellite-based observations to study cloud growth and entrainment for deep convective systems in the Tropics (e.g., Takahashi & Luo, 2012; Takahashi et al., 2017), as well as through the use of ground-based precipitation radar measurements applied to case study examples (e.g., Dual-Doppler radar; Mullendore et al., 2013; Carletta et al., 2016). However, this proxy bundles several non-adiabatic terms that impact convective plume buoyancy into a single quantity, due to the lack of observational platform constraints. The buoyancy of the rising air parcel could be affected by several processes other than entrainment, including hydrometeor drag, latent heating during hydrometeor phase changes, and nonhydrostatic pressure effects. Water loading contributes to frictional drag forces, as condensation and precipitation growth processes occur, which decreases the acceleration of the rising parcel (e.g., Jorgensen & LeMone, 1989). The significance of this contribution to convective vertical velocity remains a topic of debate (Sherwood et al., 2013; Romps & Charn, 2015). In addition, the perturbation pressure field plays a major role

in reducing the sharp gradients in vertical velocity near the cloud top (Holton, 1973; Chen & Sun, 2002).

For simplicity, we refer to this as an effective bulk entrainment proxy (ε_{proxy}) and apply these ideas to an extensive ground-based archive for cloud observations. We draw from a multi-year, multi-site record available from the U.S. Department of Energy's (DOE) Atmospheric Radiation Measurement (ARM) program that has advanced cloud sampling in remote, tropical regions (e.g., Mather & Voyles, 2013). ARM cloud radar observations are coupled with co-located, routine radiosonde launches to determine the ε_{proxy} for differing tropical environments (i.e., continental, coastal, oceanic). A detailed description of the DOE ARM sites, instruments, measurements, and study methodology are given in Section 2. Section 3 describes the regional variations of thermodynamic conditions for identified deep convective systems. Section 4 explores how environmental parameters are related to the ε_{proxy} in tropical convective clouds, and which explain the most variability in the ε_{proxy}. We provide a summary of the primary conclusions from this study in Section 5.

2 Date and Methods

2.1 ARM Sites

The ground-based measurement record from multiple U.S. DOE ARM sites (Stokes & Schwartz, 1994; Ackerman & Stokes, 2003; Mather & Voyles, 2013) provides the long-term and high-resolution observations of cloud properties and atmospheric state that form the basis of the analyses presented in this study. Our focus is on six ARM deployment sites in the Tropics, and includes fixed multi-year deployments and 1-2 year ARM Mobile Facility (AMF; Miller et al., 2016) deployments. We plot the locations and additional details for these deployments in Figure 1. Historically, the ARM program operated three fixed sites along the equator in the Tropical Western Pacific Ocean (TWP; Mather et al., 1998; Long et al., 2013, 2016), motivated by the need to sample the migration of the intertropical convergence zone (ITCZ) and the phases of the El Niño-Southern Oscillation (ENSO). The initial TWP site (TWP-C1) was established on Manus Island in Papua New Guinea, in the middle of the tropical warm pool where the environment is influenced by the Madden-Julian oscillation (MJO) and the site experiences persistent cloudiness and rainfall (e.g., McFarlane et al., 2013). The second TWP site (TWP-C2) was located

on Nauru Island in the Republic of Nauru, on the eastern edge of the tropical warm pool. This location exhibits strong variability in precipitation characteristics and convective properties, as attributed to ENSO cycles (e.g., Jensen et al., 1998; Porch et al., 2006). A third coastal site (TWP-C3) was in Darwin, Australia, which is dominantly affected by the annual Australian monsoon system (e.g., P. T. May et al., 2012; Giangrande et al., 2014).

Three additional tropical datasets were collected during recent AMF campaigns, which include one tropical-oceanic location and two tropical-continental deployments. The earliest continental-tropical site deployment was located in Niamey, Niger (NIM; Miller & Slingo, 2007), with AMF1 operations from January 2006 to January 2007 as part of the African Monsoon Multidisciplinary Analysis campaign (Lebel et al., 2003). This one-year experiment continuously measured the seasonal variations in cloud and radiation properties in Niamey, which are strongly influenced by Saharan desert dust and biomass burning during the dry seasons and frequent deep convective activity after the arrival of the West African Monsoon (e.g., Miller & Slingo, 2007; Slingo et al., 2008; Kollias et al., 2009). A second tropical-continental dataset was collected in the central Amazon basin near Manacapuru, Brazil (MAO) during the Observations and Modeling of the Green Ocean Amazon 2014-2015 (GoAmazon2014/5) Experiment from January 2014 to November 2015 (Martin et al., 2016). In the Amazonian tropical forest, the synoptic circulation patterns change across seasons impacting the convective cloud types and organization, further complicating the aerosol-cloud-precipitation interactions (e.g., Giangrande et al., 2017; Machado et al., 2018; Wang et al., 2018). Finally, a tropical-oceanic deployment of the AMF was on Gan Island, Maldives (GAN; Long, 2010, 2011), during the ARM MJO Investigation Experiment (AMIE-Gan) from October 2011 to March 2012. The GAN site is located in the middle of the Indian Ocean where the convection population and precipitation amount vary significantly according to the phases of the MJO (e.g., Yoneyama et al., 2013).

2.2 Measurements

The Active Remote Sensing of CLouds (ARSCL; Clothiaux et al., 2000; Kollias et al., 2005) value added product (ARM, 1999) is the primary dataset used in this study to identify deep convective clouds and characterize cloud properties. This product merges observations from vertically-pointing millimeter cloud radar, laser ceilometer, micropulse

lidar, and microwave radiometer to describe the cloud vertical structure at high resolution (∼10 s, ∼ 24 m). Overall, ground-based cloud radars are capable of sampling the forward anvil clouds of deep convection when there is limited attenuation in rain and/or few underlying clouds (e.g., Kollias et al., 2007). At different locations, ARM cloud radars operate at different frequencies, with 95 GHz W-band ARM Cloud Radar (WACR; Widener & Mead, 2004; Giangrande et al., 2012) at NIM and MAO, and 35 GHz Ka-band ARM Zenith Radar (KAZR or MMCR [Millimeter-wavelength Cloud Radar]; Kollias et al., 2007; Widener et al., 2012) at GAN and the three TWP sites. Additional details on radar type and location are summarized in Table 1. Although these different radars and operating wavelengths carried different beamwidths, sensitivities to clouds, and slight changes in small anvil/ice particle scattering and/or potential for gaseous attenuation or attenuation in rain, these differences do not significantly impact the determination of the bulk anvil properties of interest for this study.

The surface atmospheric conditions are provided by a collocated standard Surface Meteorological System (MET; ARM, 2013) at each ARM site. These sensors record 1-min observations of temperature, specific humidity, and rainfall rate. Depending upon the geographical area and local conditions, different types of surface sensors were deployed to measure these surface quantities. Detailed information on these sensors and additional surface variables measured at each ARM site can be found in Ritsche (2011) and Table 1. Thermodynamic profiling is available from ARM radiosondes routinely launched 1 to 6 times per day according to the site and field campaign designations (ARM, 2019). The Vaisala RS-92 radiosondes have been used as part of regular operations for ARM AMF deployments, and became a standard at all of the ARM sites since 2005 (Holdridge et al., 2011; Jensen et al., 2015). For the three TWP sites that have the longest records in the program, three generations of radiosondes (i.e., RS-80, RS-90, and RS-92) have been used and replaced since the beginning of the deployments (Holdridge et al., 2011, Table 1). For the planetary boundary layer (PBL) height, we use the estimates based on a bulk Richardson number method developed in Seibert et al. (2000) using the radiosonde measurements (Sivaraman et al., 2013; ARM, 2014).

204 ## 2.3 Methodology

205 ### *2.3.1 Case Selection*

206 Deep convective events were selected based on time-height profiles of ARSCL best-
207 estimate reflectivity (e.g., Figure 2). Selected events are required to have a cloud-top (radar
208 echo top) height greater than 10 km, with an extensive forward anvil cloud, which is de-
209 fined as extended cloud at the top and leading edge of a deep convective cloud with con-
210 tinuing observations from ground-based profiling radar for a minimum of 30 minutes and
211 having a cloud base above 5 km. These criteria are similar to previous satellite-based
212 definitions in studies by Takahashi and Luo (2012) and Takahashi et al. (2017). We lim-
213 ited our samples to the convective events that have radiosondes launched within 6 hrs
214 prior to the convective updrafts passing over the sites. Based on this visual inspection,
215 we identify 320 tropical deep convection events (listed in Appendix Table A1) that meet
216 these criteria (i.e., 11 for GAN, 23 for NIM, 36 for MAO, 173 for TWP-C1, 16 for TWP-
217 C2, 61 for TWP-C3). We plot an example of one event from 6 December, 2005 at the
218 TWP-C1 site in Figure 2, with a forward anvil cloud indicated by the black box. Note
219 that while the presence of a pronounced anvil feature intrinsically implies that we only
220 consider deeper convective events at mature to later lifecycle stages, we recognize that
221 the characteristics of convection (e.g., updraft intensity, cold pool properties, detrain-
222 ment height) can also vary significantly from updraft-dominant early mature to downdraft-
223 dominant later mature stages (e.g., Mullendore et al., 2013; Feng et al., 2018).

224 ### *2.3.2 Level of Neutral Buoyancy*

225 Pre-convection radiosondes are used to estimate thermodynamic variables follow-
226 ing parcel theory with different assumptions, considering both irreversible pseudo-adiabatic
227 and reversible moist adiabatic ascents. Ice phase is considered in the parcel model, which
228 provides an additional source of positive buoyancy above the melting level from latent
229 heat released during freezing. When assuming the air parcel experiences undiluted as-
230 cent in a pseudo-adiabatic process, we neglect hydrometeor loading. An unsaturated air
231 parcel lifted from the surface or boundary layer will eventually reach a level where it be-
232 comes saturated due to dry adiabatic cooling (i.e., the lifting condensation level, LCL).
233 As this air parcel is further lifted following the moist adiabatic lapse rate, it will rise to
234 the level of free convection (LFC) where it becomes positively buoyant and accelerates

upward. When the buoyancy decreases to zero again during its ascent, this parcel reaches the level of neutral buoyancy (LNB). As the LNB calculation is highly sensitive to the choice of the initial parcel, we performed our tests for a surface-based parcel, the most unstable parcel, and the mixed-layer parcel. The surface-based parcel is defined as the parcel at the lowest sounding data level; the most unstable parcel is defined as the parcel that has the greatest virtual temperature in the lowest 700 mb above surface; the mixing-layer parcel is defined as the parcel with properties of the mean of the boundary layer. Choosing the most unstable parcel elevates the LNB (LNB_{mu}) by 0.6 km on average compared to the surface-based LNB (LNB_{sfc}, Figure 3a), which is consistent with findings in Mullendore et al. (2013). When considering the mixed-layer parcel (in order to eliminate the enhanced heating at the surface), the mean LNB lowers dramatically (by 1.6 km compared to LNB_{mu}) as the calculation is based on the mean air parcel condition (e.g., temperature and humidity) below the PBL height. In order to investigate the limitation of pseudo-adiabatic assumption and the role of hydrometeor loading on parcel buoyancy, we incorporate reversible moist adiabatic ascent in the parcel model. Assuming reversible moist adiabatic ascent reduces buoyancy and lowers the mean LNB (LNB_{rev}) by about 2.5 km compared to the irreversible pseudo-adiabatic ascent (LNB_{mu}, Figure 3a).

2.3.3 Level of Maximum Detrainment

In reality, the convective air parcel rarely rises to the LNB before detraining from the convective cores. The buoyancy of the rising air parcel will be affected by entrainment, hydrometeor drag, latent heating during hydrometeor phase changes, and nonhydrostatic pressure effects. Through the combined influences of these processes, the level of maximum detrainment (LMD), as the altitude where most of the air mass and ice particles detrain horizontally after convective parcels decelerate, will be lower than the estimated LNB.

Following Mullendore et al. (2009) and Takahashi et al. (2017), the LMD is determined by the height of the maximum radar reflectivity within the forward anvil cloud. We calculate the bulk entrainment rate proxy, ε_{proxy} (e.g., Takahashi & Luo, 2012) as the difference between the idealized LNB and observed LMD, recalling that this proxy encompasses the effects of entrainment and other processes that contribute to the deceleration of the rising convective parcel. To avoid the noisiness in the measurements,

our first step is to average the reflectivity field within the forward anvil clouds at each height level, then locate the maximum mean reflectivity in altitude (LMD_{mean}). As a sensitivity test for this approach, we also consider the height of the maximum reflectivity in the anvil without performing the averaging step (LMD_{max}). The probability density functions of LMDs are plotted in Figure 3a as compared to the LNBs estimated for all events. The distributions of LMD_{mean} and LMD_{max} are nearly identical (mean $\sim$ 10.5 km) and lower than the corresponding LNB_{mu} with an average offset of $\sim$ 5 km, as shown in Figure 3b. These differences are comparable to previous findings based on satellite observations and parcel model calculations with the irreversible pseudo-adiabatic assumption (offset $\sim$ 4 km, Takahashi et al., 2017). This 1-km difference between satellite and ground-based methods is potentially attributed to differences in vertical resolution and attenuation between the CloudSat nadir-pointing W-band (94 GHz) Cloud Profiling Radar (Tanelli et al., 2008) and ARM ground-based profiling radars (KAZR, MMCR, and WACR; Kollias et al., 2007; Widener et al., 2012), as well as the different radar sensitivity limits when sampling anvil ice particles (e.g., higher ground-radar sensitivity). Another contributing factor is that cumulative ARM dataset properties are dominated by TWP oceanic cases that should promote relatively higher LNBs compared to other tropical sites.

Note that, the irreversible pseudo-adiabatic and reversible moist adiabatic ascents are both idealized extremes, and the real LNB falls somewhere in between. This partially explains the negative ε_{proxy} values in Figure 3b, where the LNBs are being underestimated for the cases that have hydrometeors fall out of the parcel. When using mixed-layer parcels, negative ε_{proxy} values could also be expected, since we assume the entire boundary layer is well mixed prior to convection, which represents another extreme case. In addition, the errors in the PBL height retrievals, the representativeness of the selected soundings for the local condition, and the limitations in the parcel theory such as in realistically describing the size of the initial parcel and the lifting mechanisms add additional uncertainties to the ε_{proxy} estimates.

2.3.4 Candidate Environmental Parameters

We consider a subset of candidate environmental parameters that are anticipated to be important for determining entrainment, updraft strength and regulating the overall convection evolution (e.g., Weisman & Klemp, 1984; Lucas et al., 1994b; McCaul &

Weisman, 2001; Kirkpatrick et al., 2009; Wang et al., 2019). Bulk environmental parameters such as convective available potential energy (CAPE) and vertical wind shear of the horizontal winds are important drivers of the convective lifecycle and are often components of convective parameterization schemes (e.g., Zhang & McFarlane, 1995; Gregory, 2001). Additional variables such as the convective inhibition (CIN), LFC, and the vertical distribution of cloud parcel buoyancy also have an important impact on the convective properties. In this study, a total of nine environmental quantities of interest are chosen as candidates for explaining the variability in the ε_{proxy}.

The CAPE, a measure of the work done by a parcel ascending from the LFC to the LNB, is a critical control in understanding deep convective clouds. We calculate CAPE under both irreversible pseudo-adiabatic ascent (for three different initial parcels, including the surface parcel, the most unstable parcel, and the mixed layer parcel, as CAPE_{sfc}, MUCAPE, and CAPE_{mix}, respectively) and reversible moist adiabatic ascent (for the most unstable parcel, as CAPE_{rev}). The mean CAPE_{sfc} (2357 J/kg), CAPE_{mix} (1192 J/kg), and CAPE_{rev} (985 J/kg) are much lower than the mean MUCAPE (2820 J/kg), demonstrating how this calculation of CAPE is sensitive to the thermodynamic characteristics of the initial parcel and the microphysical assumptions in the parcel model. To represent the shape of the buoyancy profile, we also calculate low-level CAPE (LCAPE) following Blanchard (1998) by integrating buoyancy through 4 km above the LFC. In addition, we also consider other environmental parameters of interest, such as the environmental temperature lapse rates (ELRs, 0-3 km and 3-6 km), the low-level mean relative humidity (RH) from surface to 5 km, and the low-level vector wind shear (surface to 5 km). These quantities are calculated from ARM radiosondes following Wang et al. (2019).

The strength of convection can be quantified in multiple ways. For this study, we use the intensity of convective cold pools as a proxy for convective strength. The convective cold pool fronts are identified by a rapid decrease of surface equivalent potential temperature ($\triangle\theta_e$) when the convective cells pass over the ARM sites, followed by a slow recovery. The cold pool strength is defined as the maximum $\triangle\theta_e$ within a 30-min time period around the maximum rainfall rate observed by ARM surface rain gauges (Schiro & Neelin, 2018; Wang et al., 2019). Note that, as in many other profiling radar/satellite/aircraft studies, we face a challenge due to the possible 'random' nature of the samples. Even though the selected cases all show mature convective signatures when passing over our

radar and surface measurements, we may not ideally sample the center of the precipitation/cold pool cores. This could potentially result in an underestimation of precipitation rate/cold pool strength.

3 Regional Comparison of Environmental Parameters

3.1 Thermodynamic Conditions

For each case, we calculate the full set of environmental parameters and generate composite profiles and site summary statistics. In Figure 4, we plot the composite skew-T log-P diagrams (using open source code MetPy; R. M. May et al., 2008 - 2020) from the radiosondes for each ARM site, once again for radiosondes launched prior to convective cores. The green solid lines in Figure 4 represent measured mean dew-point temperature profiles, while the red lines are the mean temperature profiles. The overlaid red shading on this figure indicates the mean MUCAPE, while the blue shading is the mean MUCIN. Note that the actual CAPE calculation is based on the virtual potential temperature framework, following Bryan and Fritsch (2002). In Figure 5, we plot the distributions of candidate environmental variables for each ARM site, calculated based on the most unstable parcel assuming irreversible ascent. Overall, distinct differences are observed between the associated thermodynamic conditions of interest estimated at the various tropical sites.

Among the sites considered, water vapor availability varies significantly. For the sites that are located on tropical islands (GAN, TWP-C1, TWP-C2), large amounts of moisture are available from the Pacific and/or Indian oceans, associated with higher dew-point temperatures throughout the troposphere (Figures 4a-c). On average, the median low-level RHs reach 80% at these sites in the times preceding convection (Figure 5a), which is essential to deep convection onset (e.g., Schiro & Neelin, 2019). Over the Amazon Basin (MAO, Figure 4e), sufficient moistening is also found prior to convection, as a result of the synoptic moisture advection from the Atlantic Ocean (e.g., Drumond et al., 2014; Giangrande et al., 2020, especially during the wet and transitional seasons), water vapor detrained from shallow cumulus convection, as well as the local supply through evapotranspiration (e.g., Collow et al., 2016; Schiro et al., 2016; Giangrande et al., 2017). Compared to the continental-tropical Amazon cases, the maritime continent Darwin composite (TWP-C3) shows a large spread in RH throughout the troposphere (Figure 4d, Fig-

ure 5a). This wider distribution reflects the variability through the phases of the north Australian monsoon season (active and break periods; Pope et al., 2009). During the active monsoon, the coastal TWP-C3 site experiences deep westerlies and north-westerly winds near the surface that bring substantial moisture from the Tropics to northern Australia. When the monsoon undergoes its break period, winds become easterly and less conducive to moisture transport (e.g., Evans et al., 2014). At the continental West Africa (NIM; Figure 4f) site, relatively less water vapor is available for deep convection (median low-level RH $\sim$ 70%), and the moisture availability highly depends on the onset/retreat of the West African monsoon (e.g., Mera et al., 2014).

For each site, there is strong evidence for a variety of convection that initiates and develops uniquely across different thermodynamic environments.

a) In oceanic environments, the surface/near-surface air parcel does not require significant lifting to reach saturation (median LCLs below 0.6 km, Figure 5b) as a result of the higher moisture availability within the boundary layer. The implication is that the LFCs are also lower for these cases, which helps promote more frequent convection (Figure 5c). Rising parcels under these conditions can ideally extend higher in the troposphere, as suggested by a median LNB_{mu} exceeding 15.7 km (Figure 5j). This contrasts with continental counterparts (MAO and NIM sites), which suggest a 'skinny' mean MUCAPE profile (e.g., Lucas et al., 1994b, Figures 4a-c). This LNB distribution is consistent with the LNB map generated using the A-train satellite dataset in Takahashi et al. (2017).
b) Over the West African continent (NIM), the pre-convective environment exhibits an enhanced stable layer with higher LFC (median = 2.1 km) compared to other island and continental sites (Figure 5c). This stable layer caps the boundary layer and is associated with a large amount of negative buoyancy (median MUCIN = -30 J/kg, Figures 4f, 5d). In addition, we observe steeper ELRs (median ELR_{0-3km} = 6.3 °C/km, median ELR_{3-6km} = 6.2 °C/km, Figures 5e, f) with parcel temperature largely exceeding the temperature of the surrounding air. This implies larger parcel buoyancy within the low- and mid-troposphere. As shown in Figure 4f and Figure 5g, the MUCAPE profile composite at NIM has $\sim$ 100 J/kg more integrated buoyancy at low levels (median LCAPE = 611 J/kg) compared to the oceanic composites (median LCAPE $\leq$ 484 J/kg).

c) The other continental site MAO and the coastal site TWP-C3 have slightly higher LFCs (median $\geq$ 0.8 km) than their oceanic counterparts (median $\leq$ 0.7 km) that are associated with larger ranges of CIN values. At the TWP-C3 site, the monsoon break period promotes higher CIN values compared to the active phase (e.g., M. Pope et al., 2009), which favors isolated deep convection with more intense updrafts (e.g., Keenan & Carbone, 1992). Significant shifts in MUCIN and several other environmental parameters across MAO seasons are also observed in previous studies (e.g., Giangrande et al., 2017, 2020; Wang et al., 2018). Even though substantial MUCAPE values are found at all sites before convective initiation (median $\geq$ 2651 J/kg; Figure 5h), a large percentage of the MUCAPE extremes are observed at MAO site with fatter buoyancy profiles throughout the troposphere (Figure 4e).

In terms of the mass detrainment process in deep convection (Figure 5k), every ARM tropical site exhibits a similar median LMD_{mean} ($\sim$ 10 km) but with quantifiable variability. An exception is the TWP-C3 site, showing the highest median (11.7 km) and extreme of LMD. LMD is found to be negatively correlated with low-level RH (r = -0.3, not shown), suggesting a higher LMD for cases that developed in a drier condition. However, the dependence of LMD on other environmental controls such as CAPE is much weaker ($r < 0.1$, not shown).

Consistent with the results of Takahashi and Luo (2012), the mean offsets (LNB_{mu} minus LMD_{mean}, Figure 5l) for oceanic cases are greater compared to their continental and coastal counterparts, suggesting larger ε_{proxy} in these systems. When considering surface, mixed-layer parcels, and irreversible ascent, the ε_{proxy} estimates yield similar ocean-land contrast (not shown). Note that the same microphysical assumptions are used in the parcel theory model for all the tropical sites, without considering the regional and/or climatological differences. This may add additional uncertainties in the determination of the LNB and hence the ε_{proxy} estimates.

4 Environmental Conditions Impacting Effective Bulk Entrainment

The large-scale environmental conditions interact with deep convective systems through the entrainment and mixing processes (e.g., Jensen & Del Genio, 2006; Stirling & Stratton, 2012; Böing et al., 2014). In order to explore the links between different environ-

mental factors and the ε_{proxy}, we plot the selected candidate variables discussed in previous sections as a function of the difference between LNB and LMD (Figure 6). These quantities are grouped into 1 km increments for our ε_{proxy}. To investigate whether the relationships are sensitive to the choice of the initial air parcel and the microphysical assumptions in the parcel model that determines LNB and other explanatory factors, we compare the results using the surface-based parcel (Parcel_{sfc}), the most buoyant parcel (Parcel_{mu}), and the mixed-layer parcel with irreversible pseudo-adiabatic and reversible moist adiabatic ascents. The uncertainty in LMD estimation (e.g., usage of LMD_{mean} versus LMD_{max}) definitions is also considered in the comparison.

4.1 Relationships Between the Environmental Parameters and Effective Bulk Entrainment

For the relationships between the environmental parameters and the ε_{proxy} (Figure 6), the linear correlation coefficients are found to be weak to moderate (i.e., $r \leq 0.6$). These relationships with CAPE, CIN, and LFC, to a certain extent, are sensitive to the choice of different originating air parcels, showing slightly higher correlations for quantities calculated using the surface and mixed-layer parcels (not shown) compared to the most unstable parcel. However, as correlation coefficients are intended for quantities that are linearly related, these calculations are provided as one reference, but do not fully quantify the complex relationships between entrainment and surrounding environment. Note that fully isolating entrainment from all the potential contributing factors, the perturbation pressure field in particular, is extremely difficult using existing observational datasets. However, when considering a reversible ascent of the air parcel, higher correlations are shown with CAPE, CIN, and LFC, which, to a certain extent, emphasizes the dependence of entrainment on these environmental controls.

The CAPE is positively correlated with ε_{proxy} (Figure 6a), suggesting that entrainment and the additional non-adiabatic contributions tend to be more efficient for the events that have larger CAPE ($r \sim 0.5$ with surface parcels). This is explained due to higher CAPE corresponding to a larger buoyancy term in the turbulent kinetic energy budget (e.g., S. B. Pope, 2000; Jensen & Del Genio, 2006). Figures 6b-c show a decrease in the value of ε_{proxy} when increasing the CIN (CIN increasing to greater negative values) and the LFC. One explanation for these behaviors is that the CIN and LFC negatively contribute to the total buoyancy, therefore cases with substantial CIN and/or higher LFC

tend to be less favorable for mass entraining into the convective updraft regions. The ELR also shows a negative correlation with ε_{proxy} (Figure 6d). Since a steeper ELR corresponds to a 'fatter' buoyancy profile, CAPE concentrates at lower levels and an air parcel accelerates more quickly through those levels. This faster accelerating parcel would reduce the amount of time/exposure for entrainment and other processes to occur.

We observe a steady increase in ε_{proxy} with increasing low-level RH (Figure 6e). A higher RH environment promotes entrainment through its effects on buoyancy production of the turbulent kinetic energy (Jensen & Del Genio, 2006; Lu et al., 2018; Stanfield et al., 2019). In Figure 6f, the ε_{proxy} indicates a negative weak correlation with convective cold pool strength (i.e., $\triangle\theta_e$). This result is consistent with the presence of cold pools implying the propensity of the atmosphere to promoting deeper and more intense convection/updrafts that are less impacted by entrainment (e.g., Böing et al., 2012) and other non-adiabatic processes. Besides, stronger cold pools generated by more intense convective downdrafts are anticipated to create larger eddies at the gust fronts. These larger eddies entrain less than the smaller turbulent eddies in the boundary layer (e.g., Kuang & Bretherton, 2006; Khairoutdinov & Randall, 2006).

In Figure 7, we break down these relationships for oceanic (i.e., GAN, TWP-C1, TWP-C2) and continental/coastal (i.e., NIM, MAO, TWP-C3) cases. For examples in Figure 7, only the most unstable parcel followed irreversible ascent is shown on these plots, and we only consider the LMD_{mean}, as the other previously discussed combinations yield similar results. Overall, this subset of relationships is in agreement with previous cumulative dataset arguments as shown in Figure 6. The continental/coastal events demonstrate a slightly higher correlation overall, compared to the oceanic counterparts, however, this land-ocean contrast becomes minimal when using surface parcels and/or assuming reversible moist adiabatic ascent (not shown). Note that, for surface-based calculations, the changes in correlations for continental cases are negligible, as most of the most unstable parcels are the surface parcels over the land.

Other environmental variables of interest (ELR_{0-3km}, LCL, wind shear) all show weak correlations with ε_{proxy} (not shown). The ELR_{0-3km} is positively correlated with ε_{proxy} (weak $r \sim 0.2$), since larger ELR_{0-3km} tends to promote higher CAPE ($r = 0.43$, Figure 8) in the Tropics. The LCL found to have negative correlation with ε_{proxy} (weak $r \sim$ -0.2), as it is highly related to LFC ($r = 0.68$, Figure 8). ε_{proxy} responses to wind

shear changes are complex and found to be regime-dependent, with higher correlation for the continental cases compared to oceanic counterparts (not shown). Note that the environmental conditions impact ε_{proxy} through their controls on both LNB and LMD. The CAPE and CIN are found to have a higher correlation with LNB than with LMD and the low-level RH is found to be more strongly related to LMD than to LNB (not shown).

4.2 Factors Controlling Effective Bulk Entrainment Proxy

There are several ongoing challenges related to how the entrainment and other non-adiabatic processes in deep convection respond to changes in environmental conditions, and which environmental or thermodynamic quantities of interest have the greatest predictive capabilities to inform on those processes (e.g., Hannah, 2017). For this study, we use a Random Forest (RF) method to investigate the importance of several candidate quantities in explaining the observed ε_{proxy} in deep convection. The RF regression algorithm (Breiman et al., 1984; Quinlan, 1993) is an ensemble-learning algorithm that combines a large set of regression trees. The main advantages to applying RF methods to address this question is that these methods handle non-linear parameters efficiently, require no feature scaling, and have a low overfitting risk (Breiman, 2001). We accomplish this using the open-source Scikit-learn's RF regression algorithm (toolkit from Pedregosa et al., 2011). We optimize the RF approach by tuning two important parameters, the number of regression trees and the number of inputs per node. After performing these sensitivity tests, 500 regression trees are included in the RF with 5 inputs per node, since this combination yields the lowest root mean square error for our particular application.

The RF regression algorithm reports the feature importance score for each input quantity (e.g., Breiman, 2001; Liaw & Wiener, 2002). As shown in Figure 9a, the MUCAPE and low-level RH exhibit higher feature importance scores (0.19 and 0.17) compared to other candidates, indicating these indices as more important to quantifying ε_{proxy} in tropical deep convection. This finding is consistent with the previous work by Jensen and Del Genio (2006) for tropical cumulus congestus clouds observed at Nauru (TWP-C2). Other environmental variables suggest relatively lower feature importance, with the implication that these quantities are not informative to the governing factors for the ε_{proxy} in tropical deep convective clouds. When considering calculations based on other initial

parcels (i.e., surface- and mixed-layer), CAPE always obtains the highest feature importance score compared to other environmental variables.

The feature importance scores have been separately calculated for the oceanic and continental event observations (Figures 9b-c). For the continental cases, in addition to MUCAPE and low-level RH, the vertical wind shear reports a relatively higher feature importance score. Again, this suggests that low-level wind shear provides greater importance in determining the ε_{proxy} compared to the oceanic cases. For the continental cases, one interpretation is that strong vertical wind shear promotes more interactions with the updrafts, and affects the vertical acceleration (e.g., Peters et al., 2019). When assuming reversible moist adiabatic ascent, CAPE remains the most important feature to the ε_{proxy} prediction. However, CIN is found to be equally important compared to vertical wind shear in determining ε_{proxy} for continental cases.

Note that the RF approach could potentially underestimate the contribution of certain quantities as a predictor when they are correlated with other inputs, even though this effect is somewhat reduced owing to random selection of inputs at each node creation. On the other hand, this is one of the advantages of using RF for reducing overfitting problems, since it removes features that are mostly duplicated by other features.

5 Conclusions

This study summarizes the characteristics and regional variations of the outflow heights (LNB, LMD) and, by proxy, the ε_{proxy} (LNB minus LMD) in tropical deep convective clouds. Note that, when assuming irreversible pseudo-adiabatic ascent in the LNB calculation, this ε_{proxy} includes the effects of processes other than entrainment (e.g., condensation loading and pressure perturbation forces) that also impact the buoyancy in convective updrafts. We further investigate the contribution of condensation loading by including reversible moist adiabatic ascent in the parcel model. The subsequent investigation explores how the ε_{proxy} is related to the pre-convection environmental conditions using observations obtained from six ground-based DOE ARM sites in the Tropics. These multi-year datasets provide a considerable number of cases from diverse tropical environments including long-term observations from the Tropical Western Pacific Ocean (TWP-C1, TWP-C2, TWP-C3), West Africa (NIM), the Amazon basin (MAO), and the Indian ocean (GAN).

The key findings of this study are as follows:

a) Oceanic deep convective systems occur in a moist environment (median low-level RH $\sim$ 80%) with near-surface LCL and LFC. 'Skinny' CAPE profiles are found preceding convection, with small buoyancy accumulated at low levels (median LCAPE $\sim$ 440 J/kg), which matches those observed in previous oceanic examples (e.g., Lucas et al., 1994b, 1994a).

b) Pre-convection soundings over the continent feature higher LCLs, LFCs, and steeper ELRs. These conditions lead to a more significant CIN and larger LCAPE. The most pronounced examples for this are observed for the West Africa (NIM) datasets, where the vertical wind shear is also found to be stronger. Reduced lower-tropospheric water vapor is available for the continental cases compared to their oceanic counterparts.

c) Median LNBs (using irreversible pseudo-adiabatic ascent) in oceanic events exceed 15.7 km, with the maximum height (16.2 km) at Nauru Island (TWP-C2) in the Equatorial Pacific Ocean. Assuming reversible moist adiabatic ascent lowers the mean LNB by 2.5 km. In terms of LMD, all tropical sites exhibit a similar median value ($\sim$ 10 km). The exception is the Darwin (TWP-C3) site, where the LMD extends higher and to 11.7 km on average, due to those low RH extremes. The LNB and LMD differences (i.e., ε_{proxy}) are found to be greater in oceanic cases compared to those in continental and coastal events. This finding is consistent with previous studies by Zipser (2003) and Takahashi et al. (2017).

d) The ε_{proxy} varies depending on the environmental humidity and stability. Deep convective clouds that occur during periods with larger CAPE and/or higher low-level RH tend to have larger differences between the LMD and LNB. This behavior suggests larger ε_{proxy} and more dilution of the convective updrafts for those conditions. In contrast, the suggestion is that more stable conditions with larger CIN/steeper ELR/higher LFC tend to suppress the ε_{proxy}. Similarly, we find that events that produce stronger convective cold pools at the surface apparently experience reduced ε_{proxy}. For all the parameters considered (based on application of a RF regression approach), CAPE has the highest feature importance score in determining the ε_{proxy}, followed by low-level RH. The vertical wind shear and CIN also indicate increased importance in their role in controlling ε_{proxy} for continental deep convective clouds.

This study advances our understanding of the interaction between tropical deep convection and its surrounding environment, and which atmospheric conditions are favorable for buoyancy reducing processes (e.g., entrainment) on convective updrafts. The relationships between the ε_{proxy} and environmental variables have potential uses in convection parameterization development and provide further constraints to climate models. For example, as the CAPE is by far the most important environmental control for ε_{proxy} prediction, the CAPE profile and/or amount could be used as a scaling factor for the lateral entrainment rates in the models. In addition, lateral entrainment rates that are a function of RH may be appropriate since it has been found to have the second highest feature importance in ε_{proxy} prediction.

Table 1. Information for the ARM fixed sites and AMF deployments presented in this study. See Ritsche (2011) and Holdridge et al. (2011) for more details about the sensors.

ARM Site	Location	Observation Period	Instruments (Sensors)
Gan Island, Maldives (GAN)	0°41′25.3248"S, 73°9′0.36"E; Central Indian Ocean	Oct. 2011 - Mar. 2012 ARM Madden-Julian oscillation Investigation Experiment (AMIE-Gan)	**AMF2** SONDE (RS92); MET (HMP-155 T/RH probe, Ultrasonic WS425 Wind Monitor, PTB-330 Barometer, 815-DA Optical Sci ORG, PWD22 Present Weather Detector); KAZR
Niamey, Niger (NIM)	13°28'38.28"N, 2°10'32.88"E; West African	Jan. 2006 - Jan. 2007 African Monsoon Multidisciplinary Analysis campaign	**AMF1** SONDE (RS92); MET (HMP-45D T/RH probe, 05106 Wind Monitor, PTB-220 Barometer, 815 Optical Sci ORG, PWD22); WACR
Manacapuru, Brazil (MAO)	3°12'46.692"S, 60°35'53.16"W; Central Amazon Basin	Jan. 2014 - Nov. 2015 Observations and Modeling of the Green Ocean Amazon 2014-2015 Experiment (GoAmazon2014/5)	**AMF1** SONDE (RS92); MET (HMP-45D T/RH probe, 05106 Wind Monitor, PTB-220 Barometer, 815 Optical Sci ORG, PWD22); WACR
Manus Island, Papua New Guinea (TWP-C1)	2°3'36"S, 147°25'30"E; Middle of the Tropical Warm Pool	Jan. 1996 - Aug. 2014 (Period from Jul. 1999 to Feb. 2011 is considered in this study)	SONDE (RS80, RS90, RS92); MET (HMP-45D T/RH probe, 05106 Wind Monitor, PWD22, 815 Optical Sci ORG and RIMCO 7499 TBRG); MMCR/KAZR (After Mar. 2011)
Nauru Island, Republic of Nauru (TWP-C2)	0°31'15.6"S, 166°54'57.6"E; Eastern Edge of the Warm Pool	Jan. 1998 - Aug. 2013 (Period from Jun. 2001 to Apr. 2007 is considered in this study)	SONDE (RS80, RS90, RS92); MET (HMP-45D T/RH probe, 05106 Wind Monitor, 815 Optical Sci ORG and RIMCO 7499 TBRG); MMCR
Darwin, Australia (TWP-C3)	12°25'30"S, 130°53'31.2"E; Australia North Coast	Jan. 2002 - Dec. 2014	SONDE (RS80, RS90, RS92); MET (HMP-45D T/RH probe, 05106 Wind Monitor, PWD22, 815 Optical Sci ORG and RIMCO 7499 TBRG); MMCR/KAZR (After Jan. 2011)

ARM=Atmospheric Radiation Measurement; AMF=ARM Mobile Facility; MET=The ARM Surface Meteorology Systems; KAZR=The Ka-band ARM Zenith Radar; WACR=The 95 GHz W-band ARM Cloud Radar; SONDE=Balloon-borne sounding system; MMCR=Millimeter-wavelength Cloud Radar.

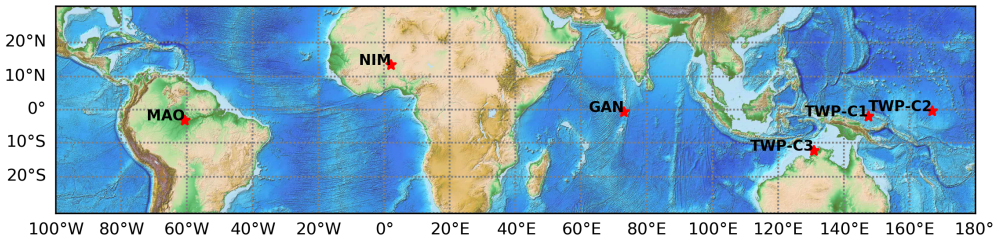

Figure 1. Map of the Atmospheric Radiation Measurement (ARM) fixed sites at Manus Island (TWP-C1), Nauru Island (TWP-C2) and Darwin (TWP-C3), Australia, and the ARM Mobile Facility deployments in Niamey, Niger (NIM), Gan Island, Maldives (GAN), and Manacapuru, Brazil (MAO).

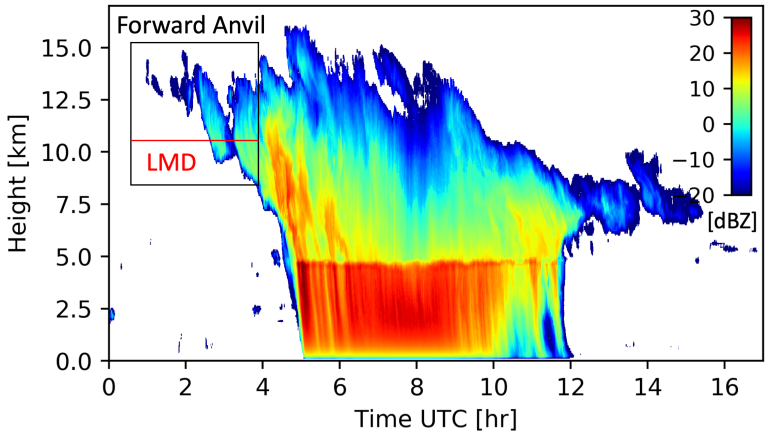

Figure 2. Deep convective example observed by an ARM profiling radar (MMCR) on 06 December, 2005 at the ARM TWP-C1 site in Manus. The colors are the radar reflectivity field in dBZ. The red line indicates the level of maximum detrainment (LMD) and the black box is the identified forward anvil. ARM=Atmospheric Radiation Measurement, MMCR=Millimeter-wavelength Cloud Radar.

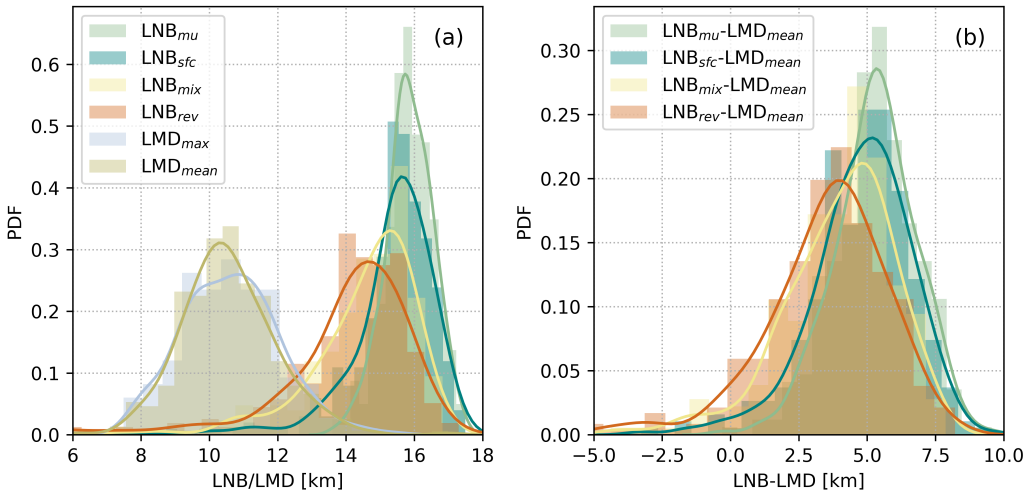

Figure 3. (a) Probability density functions (PDFs) of the levels of neutral buoyancy (LNBs) estimated based on surface parcel (LNB_{sfc}), the most unstable parcel in the low levels (LNB_{mu}), and the mixed-layer parcel within the boundary layer (LNB_{mix}) assuming irreversible pseudo-adiabatic ascent, and the levels of maximum detrainment (LMD_{max}, LMD_{mean}) estimated from profiling radar. LNB_{rev} is estimated assuming reversible moist adiabatic ascent in the parcel model for the most unstable parcel. (b) PDFs of LNBs minus LMD_{mean} (ε_{proxy}). The solid lines are the PDFs calculated using gaussian kernel density estimation.

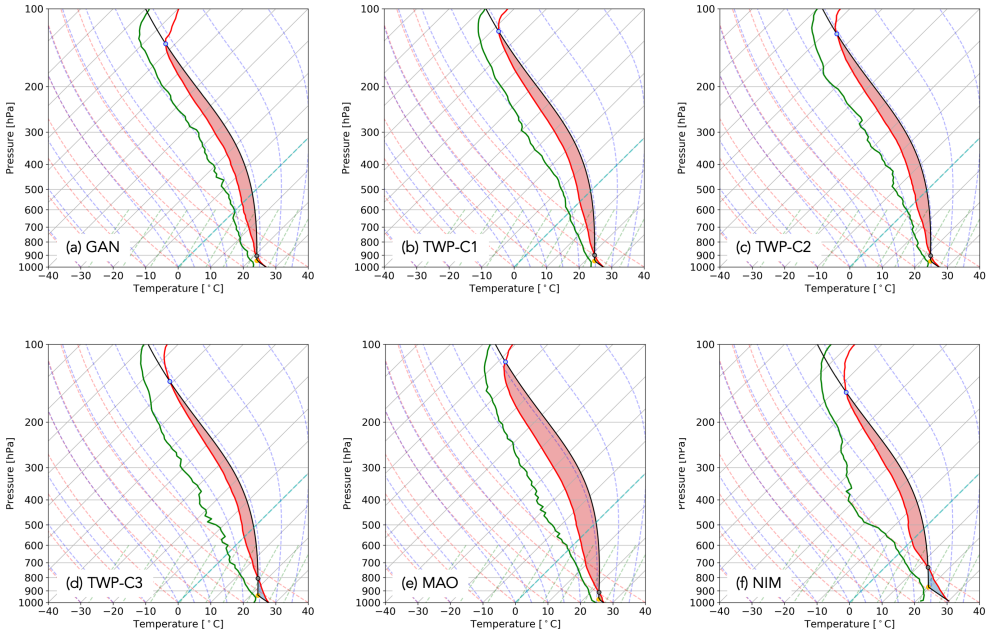

Figure 4. Composite pre-storm soundings for each site. The red line is the mean dry bulb temperature, the green line is the mean dew-point temperature and the black line represents the mean dry bulb temperature of a rising parcel originating from the most unstable layer. The red shading represents the most unstable convective available potential energy (MUCAPE), while blue is the most unstable convective inhibition (MUCIN). The grey dots indicate the levels of free convection (LFCs), the blue dots are the levels of neutral buoyancy (LNBs), and the yellow dots are the lifting condensation levels (LCLs).

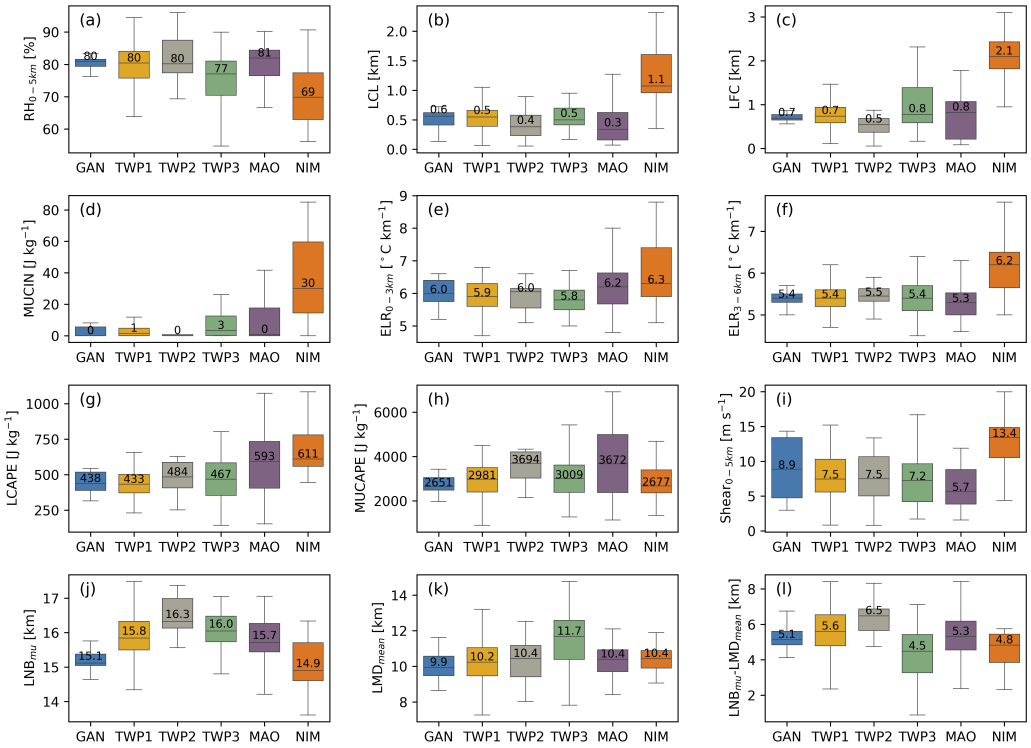

Figure 5. Box and whisker plots of environmental variables for each site (parcel follows irreversible pseudo-adiabatic ascent and ice processes are included). The middle lines show the median values. The colored boxes represent observations inside the 25th - 75th percentile range. The whiskers show the 10th/90th percentile value. RH=Relative Humidity; LCL=Lifting Condensation Level; LFC=Level of Free Convection; MUCIN=Most Unstable Convective Inhibition; ELR=Environmental Lapse Rate; LCAPE=Low-level Convective Available Potential Energy; MUCAPE= Most Unstable Convective Available Potential Energy; LNB=Level of Neutral Buoyancy; LMD=Level of Maximum Detrainment.

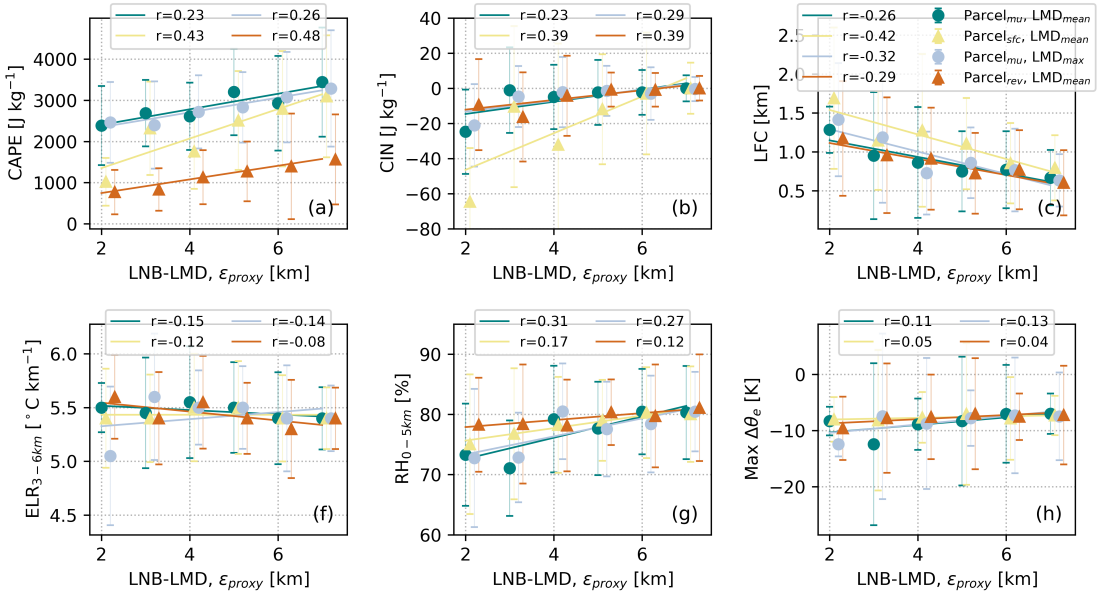

Figure 6. Mean environmental variables for each bin plotted as a function of ε_{proxy} (LNB minus LMD) for all sites. Bins have a width of 1 km, and error bars represent ±1 standard deviation. Solid lines are the linear least squares regression fits. All the correlations pass the significance tests, except for $\triangle\theta_e$ - ε_{proxy} relationships for parcel$_{sfc}$ and parcel$_{rev}$. CAPE=Convective Available Potential Energy; CIN=Convective Inhibition; LFC=Level of Free Convection; RH=Relative Humidity; ELR=Environmental Lapse Rate; LNB=Level of Neutral Buoyancy; LMD=Level of Maximum Detrainment.

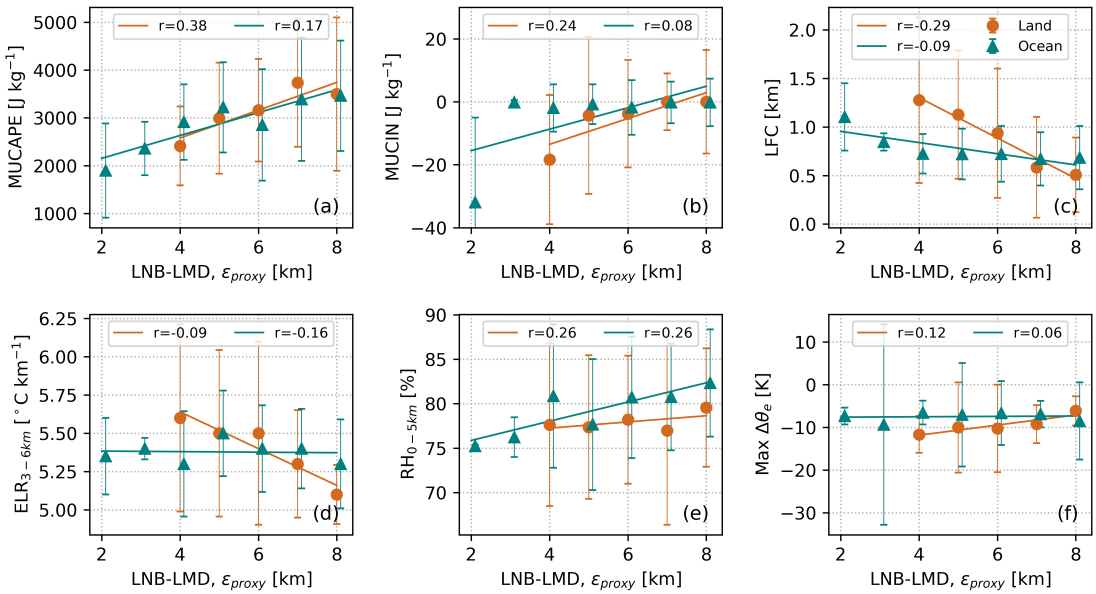

Figure 7. Same as Figure 6, but for continental, coastal (dark orange) and oceanic events (green), separately, using the most unstable air parcel and LMD_{mean} and assuming irreversible ascent.

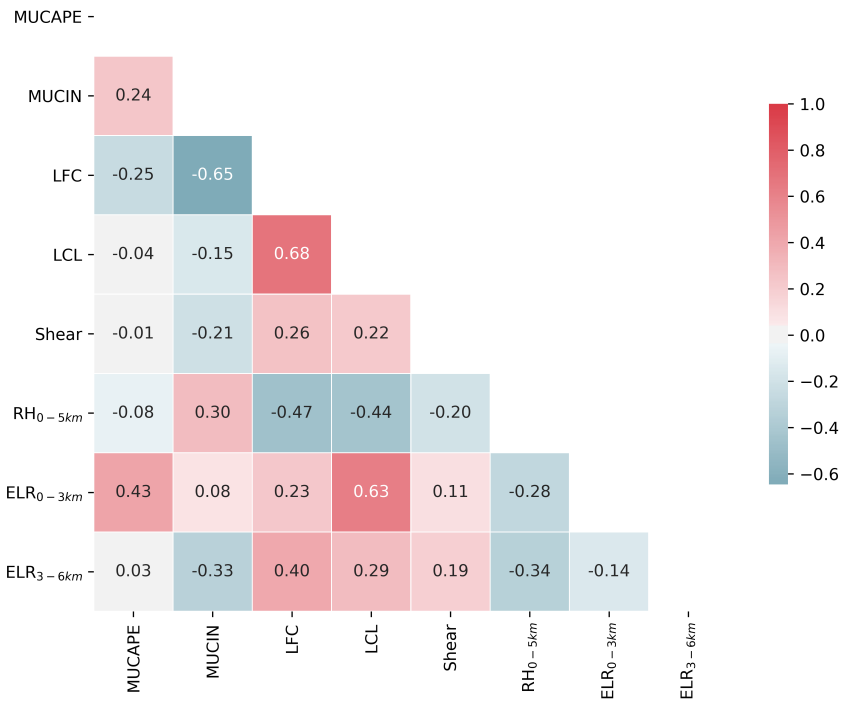

Figure 8. Correlation matrix for environmental variables (parcel follows irreversible pseudo-adiabatic ascent).

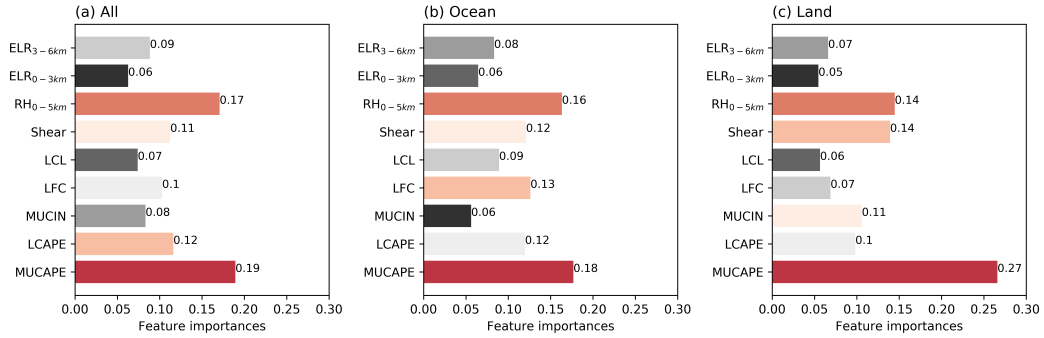

Figure 9. Bar diagram of the feature importance scores estimated for 9 environmental variables using a Random Forest algorithm to predict ε_{proxy} for (a) all the deep convective cases; (b) for only oceanic cases; (c) for only continental cases. The input and output variables are calculated using the most unstable air parcel and assuming irreversible pseudo-adiabatic ascent and LMD_{mean}. ELR=Environmental Lapse Rate; RH=Relative Humidity; LCL=Lifting Condensation Level; LFC=Level of Free Convection; MUCIN=Most Unstable Convective Inhibition; LCAPE=Low-level Convective Available Potential Energy; MUCAPE=Most Unstable Convective Available Potential Energy.

595 **Appendix A List of Selected Tropical Deep Convective Cases**

Table A1. Selected tropical deep convective cases in this study.

ARM Site	Case (MM/DD/YY)
GAN	10/16/11, 10/18/11, 10/20/11, 10/28/11, 10/31/11, 11/17/11, 11/22/11, 11/26/11, 12/22/11, 12/23/11, 01/14/12
NIM	06/27/06, 07/05/06, 07/06/06, 07/11/06, 07/19/06, 07/20/06, 07/22/06, 07/25/06, 07/26/06, 07/31/06, 08/03/06, 08/06/06, 08/07/06, 08/08/06, 08/11/06, 08/14/06, 08/18/06, 08/22/06, 08/28/06, 09/08/06, 09/10/06, 09/12/06, 09/19/06
MAO	04/01/14, 04/21/14, 04/25/14, 05/01/14, 05/09/14, 06/06/14, 06/16/14, 10/15/14, 10/25/14, 11/04/14, 11/15/14, 11/22/14, 11/27/14, 12/05/14, 01/31/15, 03/01/15, 03/16/15, 03/17/15, 03/23/15, 04/13/15, 04/17/15, 04/20/15, 04/24/15, 04/25/15, 05/14/15, 05/23/15, 05/30/15, 06/02/15, 08/26/15, 08/30/15, 09/15/15, 10/12/15, 10/25/15, 11/03/15, 11/04/15, 11/20/15
TWP-C1	07/02/1999, 07/11/1999, 08/09/1999, 03/31/00, 05/19/00, 06/23/00, 06/24/00, 06/27/00, 08/13/00, 10/22/00, 05/28/01, 06/23/01, 07/29/01, 03/05/03, 04/27/03, 06/12/03, 06/15/03, 06/22/03, 07/06/03, 07/14/03, 08/07/03, 08/09/03, 08/11/03, 08/18/03, 08/21/03, 08/23/03, 08/24/03, 09/06/03, 09/10/03, 09/13/03, 09/15/03, 09/20/03, 09/27/03, 10/02/03, 10/03/03, 10/13/03, 11/10/03, 11/22/03, 12/23/03, 12/28/03, 12/29/03, 01/03/04, 01/15/04, 01/23/04, 01/31/04, 02/05/04, 02/10/04, 02/19/04, 03/03/04, 03/16/04, 04/11/04, 04/27/04, 05/12/04, 06/04/04, 06/09/04, 06/14/04, 07/10/04, 07/16/04, 07/26/04, 09/29/04, 10/03/04, 10/10/04, 10/24/04, 10/30/04, 12/02/04, 12/20/04, 01/01/05, 01/03/05, 01/17/05, 01/18/05, 01/22/05, 01/23/05, 02/03/05, 05/27/05, 05/31/05, 06/10/05, 11/25/05, 11/26/05, 12/06/05, 12/07/05, 12/21/05, 02/11/06, 03/11/06, 03/30/06, 07/23/06, 10/23/06, 11/02/06, 11/24/06, 01/05/07, 01/26/07, 02/22/07, 03/05/07, 03/27/07, 03/30/07, 05/02/07, 05/08/07, 05/30/07, 02/16/08, 03/21/08, 06/19/08, 07/16/08, 10/31/08, 03/11/09, 04/16/09, 04/23/09, 04/25/09, 03/08/10, 03/13/10, 03/29/10, 03/31/10, 04/20/10, 07/27/10, 02/04/11, 03/16/11, 03/20/11, 03/23/11, 03/26/11, 03/30/11, 04/05/11, 04/14/11, 04/17/11, 04/21/11, 04/25/11, 06/17/11, 06/20/11, 07/17/11, 07/18/11, 07/23/11, 08/14/11, 08/26/11, 09/18/11, 09/19/11, 09/20/11, 09/30/11, 10/06/11, 10/10/11, 11/17/11, 11/23/11, 12/09/11, 12/12/11, 12/20/11, 01/05/12, 01/06/12, 01/09/12, 01/26/12, 01/30/12, 01/31/12, 02/09/12, 03/05/12, 03/16/12, 03/21/12, 03/28/12, 04/07/12, 04/15/12, 04/30/12, 05/08/12, 05/24/12, 07/25/13, 08/01/13, 08/09/13, 08/12/13, 08/14/13, 08/21/13, 08/23/13, 09/09/13, 09/21/13, 10/08/13, 10/26/13, 11/06/13, 11/07/13, 11/09/13, 11/14/13, 11/19/13
TWP-C2	06/24/01, 07/23/01, 08/09/01, 09/14/01, 11/28/01, 12/19/01, 01/24/02, 01/29/02, 03/03/02, 06/19/02, 06/20/02, 01/14/05, 10/26/05, 12/02/06, 12/19/06, 04/21/07
TWP-C3	01/13/03, 01/14/03, 01/24/03, 11/09/05, 11/10/05, 12/09/05, 01/06/06, 03/08/06, /03/11/06, 03/29/06, 04/13/06, 12/25/06, 01/21/07, 01/27/07, 01/31/07, 02/12/07, 03/19/07, 01/27/08, 02/08/08, 02/11/08, 02/16/08, 03/15/08, 11/21/08, 12/04/08, 12/09/08, 02/27/09, 12/07/10, 01/09/11, 02/22/11, 03/24/11, 03/25/11, 04/09/11, 12/20/11, 01/13/12, 01/17/12, 01/21/12, 01/22/12, 01/29/12, 02/08/12, 02/26/12, 03/02/12, 03/05/12, 03/10/12, 05/02/12, 01/12/13, 01/14/13, 01/27/13, 01/31/13, 02/11/13, 02/14/13, 03/10/13, 03/12/13, 03/15/13, 03/16/13, 03/28/13, 04/01/13, 05/23/13, 10/14/13, 12/24/13, 01/05/14, 04/27/14

Acknowledgments

This project was supported by the U.S. Department of Energy (DOE) Atmospheric System Research (ASR) program, the Climate Model Development and Validation (CMDV) program, and the Office of Workforce Development for Teachers and Scientists (WDTS) under the Science Undergraduate Laboratory Internships Program (SULI). This paper has been authored by employees of Brookhaven Science Associates, LLC, under contract DE-SC0012704 with the U.S. DOE. The publisher by accepting the paper for publication acknowledges that the U.S. Government retains a nonexclusive, paid-up, irrevocable, worldwide license to publish or reproduce the published form of this paper, or allow others to do so, for United States Government purposes. We also acknowledge the Atmospheric Radiation Measurement program, a user facility of the U.S. DOE, Office of Science, sponsored by the Office of Biological and Environmental Research, and support from the ASR program of that office. Dr. Mullendore was partially supported by National Aeronautics and Space Administration (NASA) Grant 80NSSC19K0343. Dr. Luo would like to acknowledge support by NASA grants 80NSSC17K0197 and 80NSSC20K0089.

The authors declare that there is no conflict of interest regarding the publication of this article.

Data availability: All ARM data sets used for this study are available through the ARM discovery website `https://adc.arm.gov/discovery/`.

a) The Active Remote Sensing of CLouds (ARSCL) products: `https://adc.arm.gov/discovery/#v/results/s/finst::kazrarscl/fdpl::ganarsclkazr1kolliasM1.c1/fdpl::twparsclkazr1kolliasC1.c1/fdpl::twparsclkazr1kolliasC3.c1` `https://adc.arm.gov/discovery/#v/results/s/finst::arscl/fdpl::twparscl1clothC1.c1/fdpl::twparscl1clothC2.c1/fdpl::twparscl1clothC3.c1` `https://adc.arm.gov/discovery/#v/results/s/finst::wacrarscl/fdpl::maoarsclwacr1kolliasM1.c1/fdpl::nimarsclwacr1kolliasM1.c1`
b) The Surface Meteorology Systems (MET): `https://adc.arm.gov/discovery/#v/results/s/finst::met/fdpl::ganmetM1.b1/fdpl::nimmetM1.b1/fdpl::twpmetC1.b1/fdpl::twpmetC2.b1/fdpl::twpmetC3.b1/fdpl::maometM1.b1/fdpl::nimmetS1.b1`
c) Radiosondes: `https://adc.arm.gov/discovery/#v/results/s/finst::sonde/fdpl::gansondewnpnM1.b1/fdpl::maosondewnpnM1.b1/fdpl::nimsondewnpnM1`

628 .b1/fdpl::twpsondewnpnC1.a1/fdpl::twpsondewnpnC1.b1/fdpl::twpsondewnpnC2
629 .a1/fdpl::twpsondewnpnC2.b1/fdpl::twpsondewnpnC3.b1
630 d) The Planetary Boundary Layer Height (PBLHT): https://www.archive.arm.gov/
631 discovery/#v/results/s/fdsc::pblhtsonde1mcfarl/fsite::twp.P/fsite::
632 gan.M/fsite::mao.M/fsite::nim.M

633 Python machine learning codes were provided by Scikit-learn, as from Pedregosa
634 et al., (2011).

References

Ackerman, T. P., & Stokes, G. M. (2003). The atmospheric radiation measurement program. *Phys. Today*, *56*, 38-44. doi: 10.1063/1.1554135

Anber, U., Giangrande, S. E., Donner, L. J., & Jensen, M. P. (2019). Updraft constraints on entrainment: Insights from amazonian deep convection. *Journal of the Atmospheric Sciences*, *76*(8), 2429-2442. Retrieved from `https://doi.org/10.1175/JAS-D-18-0234.1` doi: 10.1175/JAS-D-18-0234.1

ARM. (1999). Active remotely-sensed cloud locations (rhbarscl1cloth). 2011-10-01 to 2012-03-31, arm mobile facility (gan) gan airport, gan island, maldives; amf2 (m1); 1999-07-01 to 2011-02-28, tropical western pacific (twp) central facility, manus i., png (c1); 2001-06-01 to 2007-04-30, tropical western pacific (twp) central facility, nauru island (c2); 2003-01-01 to 2014-04-30, tropical western pacific (twp) central facility, darwin, australia (c3); 2014-01-01 to 2015-11-30, arm mobile facility (mao) manacapuru, amazonas, brazil; amf1 (m1); 2006-01-01 to 2007-01-31, arm mobile facility (nim) niamey, niger (m1). *ARM Data Center*. Retrieved from `http://dx.doi.org/10.5439/1350682` (Compiled by S. Giangrande and K. Johnson. Data set accessed 2019-04-01) doi: 10.5439/1350682

ARM. (2013). Surface meteorological instrumentation (met). 2011-10-01 to 2012-03-31, arm mobile facility (gan) gan airport, gan island, maldives; amf2 (m1); 1999-07-01 to 2011-02-28, tropical western pacific (twp) central facility, manus i., png (c1); 2001-06-01 to 2007-04-30, tropical western pacific (twp) central facility, nauru island (c2); 2003-01-01 to 2014-04-30, tropical western pacific (twp) central facility, darwin, australia (c3); 2014-01-01 to 2015-11-30, arm mobile facility (mao) manacapuru, amazonas, brazil; amf1 (m1); 2006-01-01 to 2007-01-31, arm mobile facility (nim) niamey, niger (m1). *ARM Data Center*. Retrieved from `http://dx.doi.org/10.5439/1025220` (Compiled by J. Kyrouac, M. Ritsche, N. Hickmon and D. Holdridge. Data set accessed 2019-04-01) doi: 10.5439/1025220

ARM. (2014). Planetary boundary layer height (pblhtsonde1mcfarl). 2011-10-01 to 2012-03-31, arm mobile facility (gan) gan airport, gan island, maldives; amf2 (m1); 1999-07-01 to 2011-02-28, tropical western pacific (twp) central facility, manus i., png (c1); 2001-06-01 to 2007-04-30, tropical western pacific (twp)

central facility, nauru island (c2); 2003-01-01 to 2014-04-30, tropical western pacific (twp) central facility, darwin, australia (c3); 2014-01-01 to 2015-11-30, arm mobile facility (mao) manacapuru, amazonas, brazil; amf1 (m1); 2006-01-01 to 2007-01-31, arm mobile facility (nim) niamey, niger (m1). *ARM Data Center*. Retrieved from http://dx.doi.org/10.5439/1150253 (Compiled by L. Riihimaki and C. Sivaraman. Data set accessed 2019-04-01) doi: 10.5439/1150253

ARM. (2019). Balloon-borne sounding system (sondewnpn). 2011-10-01 to 2012-03-31, arm mobile facility (gan) gan airport, gan island, maldives; amf2 (m1); 1999-07-01 to 2011-02-28, tropical western pacific (twp) central facility, manus i., png (c1); 2001-06-01 to 2007-04-30, tropical western pacific (twp) central facility, nauru island (c2); 2003-01-01 to 2014-04-30, tropical western pacific (twp) central facility, darwin, australia (c3); 2014-01-01 to 2015-11-30, arm mobile facility (mao) manacapuru, amazonas, brazil; amf1 (m1); 2006-01-01 to 2007-01-31, arm mobile facility (nim) niamey, niger (m1). *ARM Data Center*. Retrieved from http://dx.doi.org/10.5439/1021460 (Compiled by D. Holdridge, R. Coulter, D. Holdridge, M. Ritsche, R. Coulter, J. Kyrouac and E. Keeler. Data set accessed 2019-04-01) doi: 10.5439/1021460

Barnes, G. M., Fankhauser, J. C., & Browning, W. D. (1996). Evolution of the vertical mass flux and diagnosed net lateral mixing in isolated convective clouds. *Monthly Weather Review*, *124*(12), 2764-2784. Retrieved from https://doi.org/10.1175/1520-0493(1996)124<2764:EOTVMF>2.0.CO;2 doi: 10.1175/1520-0493(1996)124⟨2764:EOTVMF⟩2.0.CO;2

Blanchard, D. O. (1998). Assessing the vertical distribution of convective available potential energy. *Weather and Forecasting*, *13*(3), 870-877. Retrieved from https://doi.org/10.1175/1520-0434(1998)013<0870:ATVDOC>2.0.CO;2 doi: 10.1175/1520-0434(1998)013⟨0870:ATVDOC⟩2.0.CO;2

Breiman, L. (2001). Random forests. *Machine Learning*, *45*, 5–32. doi: 10.1023/A:1010933404324

Breiman, L., Friedman, J. H., Olshen, R. A., & Stone, C. J. (1984). *Classification and regression trees*. Monterey, CA: Wadsworth and Brooks, Cole Advanced Books and Software. Retrieved from https://cds.cern.ch/record/2253780

Bretherton, C. S., McCaa, J. R., & Grenier, H. (2004). A new parameteri-

zation for shallow cumulus convection and its application to marine subtropical cloud-topped boundary layers. part i: Description and 1d results. *Monthly Weather Review*, *132*(4), 864-882. Retrieved from https://doi.org/10.1175/1520-0493(2004)132<0864:ANPFSC>2.0.CO;2 doi: 10.1175/1520-0493(2004)132⟨0864:ANPFSC⟩2.0.CO;2

Bretherton, C. S., & Smolarkiewicz, P. K. (1989). Gravity waves, compensating subsidence and detrainment around cumulus clouds. *Journal of the Atmospheric Sciences*, *46*(6), 740-759. Retrieved from https://doi.org/10.1175/1520-0469(1989)046<0740:GWCSAD>2.0.CO;2 doi: 10.1175/1520-0469(1989)046⟨0740:GWCSAD⟩2.0.CO;2

Bryan, G. H., & Fritsch, J. M. (2002). A benchmark simulation for moist nonhydrostatic numerical models. *Monthly Weather Review*, *130*(12), 2917-2928. Retrieved from https://doi.org/10.1175/1520-0493(2002)130<2917:ABSFMN>2.0.CO;2 doi: 10.1175/1520-0493(2002)130⟨2917:ABSFMN⟩2.0.CO;2

Böing, S. J., Jonker, H. J. J., Nawara, W. A., & Siebesma, A. P. (2014). On the deceiving aspects of mixing diagrams of deep cumulus convection. *Journal of the Atmospheric Sciences*, *71*(1), 56-68. Retrieved from https://doi.org/10.1175/JAS-D-13-0127.1 doi: 10.1175/JAS-D-13-0127.1

Böing, S. J., Siebesma, A. P., Korpershoek, J. D., & Jonker, H. J. J. (2012). Detrainment in deep convection. *Geophysical Research Letters*, *39*(20). Retrieved from https://agupubs.onlinelibrary.wiley.com/doi/abs/10.1029/2012GL053735 doi: 10.1029/2012GL053735

Carletta, N. D., Mullendore, G. L., Starzec, M., Xi, B., Feng, Z., & Dong, X. (2016). Determining the best method for estimating the observed level of maximum detrainment based on radar reflectivity. *Monthly Weather Review*, *144*(8), 2915-2926. Retrieved from https://doi.org/10.1175/MWR-D-15-0427.1 doi: 10.1175/MWR-D-15-0427.1

Chen, S. H., & Sun, W.-Y. (2002, 02). A one-dimensional time dependent cloud model. *Journal of the Meteorological Society of Japan*, *80*, 99-118. doi: 10.2151/jmsj.80.99

Clothiaux, E. E., Ackerman, T. P., Mace, G. G., Moran, K. P., Marchand, R. T., Miller, M. A., & Martner, B. E. (2000). Objective determination of cloud heights and radar reflectivities using a combination of active remote sensors at

the arm cart sites. *Journal of Applied Meteorology*, *39*(5), 645-665. Retrieved from https://doi.org/10.1175/1520-0450(2000)039<0645:ODOCHA>2.0.CO;2 doi: 10.1175/1520-0450(2000)039⟨0645:ODOCHA⟩2.0.CO;2

Cohen, C. (2000). A quantitative investigation of entrainment and detrainment in numerically simulated cumulonimbus clouds. *Journal of the Atmospheric Sciences*, *57*(10), 1657-1674. Retrieved from https://doi.org/10.1175/1520-0469(2000)057<1657:AQIOEA>2.0.CO;2 doi: 10.1175/1520-0469(2000)057⟨1657:AQIOEA⟩2.0.CO;2

Collow, A. B. M., Miller, M. A., & Trabachino, L. C. (2016). Cloudiness over the amazon rainforest: Meteorology and thermodynamics. *Journal of Geophysical Research: Atmospheres*, *121*(13), 7990-8005. Retrieved from https://agupubs.onlinelibrary.wiley.com/doi/abs/10.1002/2016JD024848 doi: 10.1002/2016JD024848

Dawe, J. T., & Austin, P. H. (2011). Interpolation of les cloud surfaces for use in direct calculations of entrainment and detrainment. *Monthly Weather Review*, *139*(2), 444-456. Retrieved from https://doi.org/10.1175/2010MWR3473.1 doi: 10.1175/2010MWR3473.1

Del Genio, A. D., & Wu, J. (2010). The role of entrainment in the diurnal cycle of continental convection. *Journal of Climate*, *23*(10), 2722-2738. Retrieved from https://doi.org/10.1175/2009JCLI3340.1 doi: 10.1175/2009JCLI3340.1

Del Genio, A. D., Wu, J., & Chen, Y. (2012). Characteristics of mesoscale organization in wrf simulations of convection during twp-ice. *Journal of Climate*, *25*(17), 5666-5688. doi: 10.1175/JCLI-D-11-00422.1

Derbyshire, S. H., Beau, I., Bechtold, P., Grandpeix, J.-Y., Piriou, J.-M., Redelsperger, J.-L., & Soares, P. M. M. (2004). Sensitivity of moist convection to environmental humidity. *Quarterly Journal of the Royal Meteorological Society*, *130*(604), 3055-3079. Retrieved from https://rmets.onlinelibrary.wiley.com/doi/abs/10.1256/qj.03.130 doi: 10.1256/qj.03.130

de Rooy, W. C., & Pier Siebesma, A. (2010). Analytical expressions for entrainment and detrainment in cumulus convection. *Quarterly Journal of the Royal Meteorological Society*, *136*(650), 1216-1227. Retrieved from https://rmets.onlinelibrary.wiley.com/doi/abs/10.1002/qj.640 doi: 10.1002/qj.640

Drumond, A., Marengo, J., Ambrizzi, T., Nieto, R., Moreira, L., & Gimeno, L. (2014). The role of the amazon basin moisture in the atmospheric branch of the hydrological cycle: a lagrangian analysis. *Hydrology and Earth System Sciences*, *18*(7), 2577–2598. Retrieved from https://www.hydrol-earth-syst-sci.net/18/2577/2014/ doi: 10.5194/hess-18-2577-2014

Evans, S., Marchand, R., & Ackerman, T. (2014). Variability of the australian monsoon and precipitation trends at darwin. *Journal of Climate*, *27*(22), 8487-8500. Retrieved from https://doi.org/10.1175/JCLI-D-13-00422.1 doi: 10.1175/JCLI-D-13-00422.1

Feng, Z., Leung, L. R., Houze, R. A., Hagos, S., Hardin, J., Yang, Q., ... Fan, J. (2018). Structure and evolution of mesoscale convective systems: Sensitivity to cloud microphysics in convection-permitting simulations over the united states. *Journal of Advances in Modeling Earth Systems*, *10*(7), 1470-1494. doi: 10.1029/2018MS001305

Fritsch, J. M., Kane, R. J., & Chelius, C. R. (1986). The contribution of mesoscale convective weather systems to the warm-season precipitation in the united states. *Journal of Climate and Applied Meteorology*, *25*(10), 1333-1345. doi: 10.1175/1520-0450(1986)025⟨1333:TCOMCW⟩2.0.CO;2

Giangrande, S. E., Bartholomew, M. J., Pope, M., Collis, S., & Jensen, M. P. (2014, 5). A summary of precipitation characteristics from the 2006–11 northern australian wet seasons as revealed by arm disdrometer research facilities (darwin, australia). *Journal of Applied Meteorology and Climatology*, *53*(5). doi: 10.1175/JAMC-D-13-0222.1

Giangrande, S. E., Feng, Z., Jensen, M. P., Comstock, J. M., Johnson, K. L., Toto, T., ... Martin, S. T. (2017). Cloud characteristics, thermodynamic controls and radiative impacts during the observations and modeling of the green ocean amazon (goamazon2014/5) experiment. *Atmospheric Chemistry and Physics*, *17*(23), 14519–14541. doi: 10.5194/acp-17-14519-2017

Giangrande, S. E., Luke, E. P., & Kollias, P. (2012). Characterization of vertical velocity and drop size distribution parameters in widespread precipitation at arm facilities. *Journal of Applied Meteorology and Climatology*, *51*(2), 380-391. Retrieved from https://doi.org/10.1175/JAMC-D-10-05000.1 doi: 10.1175/JAMC-D-10-05000.1

Giangrande, S. E., Wang, D., & Mechem, D. B. (2020). Cloud regimes over the amazon basin: Perspectives from the goamazon2014/5 campaign. *Atmospheric Chemistry and Physics Discussions*, *2020*, 1–36. Retrieved from https://www.atmos-chem-phys-discuss.net/acp-2020-67/ doi: 10.5194/acp-2020-67

Gregory, D. (2001, Jan). Estimation of entrainment rate in simple models of convective clouds. *Quarterly Journal of the Royal Meteorological Society*, *127*(571), 53-72. doi: 10.1002/qj.49712757104

Guo, X., Lu, C., Zhao, T., Zhang, G., & Liu, Y. (2015). An observational study of entrainment rate in deep convection. *Atmosphere*, *6*(9), 1362-1376. Retrieved from https://doi.org/10.3390/atmos6091362

Hannah, W. M. (2017). Entrainment versus dilution in tropical deep convection. *Journal of the Atmospheric Sciences*, *74*(11), 3725-3747. Retrieved from https://doi.org/10.1175/JAS-D-16-0169.1 doi: 10.1175/JAS-D-16-0169.1

Hannah, W. M., & Maloney, E. D. (2011). The role of moisture–convection feedbacks in simulating the madden–julian oscillation. *Journal of Climate*, *24*(11), 2754-2770. Retrieved from https://doi.org/10.1175/2011JCLI3803.1 doi: 10.1175/2011JCLI3803.1

Hartmann, D. L., Holton, J. R., & Fu, Q. (2001). The heat balance of the tropical tropopause, cirrus, and stratospheric dehydration. *Geophysical Research Letters*, *28*(10), 1969-1972. Retrieved from https://agupubs.onlinelibrary.wiley.com/doi/abs/10.1029/2000GL012833 doi: 10.1029/2000GL012833

Hartmann, D. L., & Larson, K. (2002). An important constraint on tropical cloud - climate feedback. *Geophysical Research Letters*, *29*(20), 12-1-12-4. Retrieved from https://agupubs.onlinelibrary.wiley.com/doi/abs/10.1029/2002GL015835 doi: 10.1029/2002GL015835

Holdridge, D., Prell, J., Ritsche, M., & Coulter, R. (2011). *Balloon-borne sounding system (sonde) handbook* (DOE/SC-ARM/TR-029). U.S. Department of Energy.

Holton, J. R. (1973). A one-dimensional cumulus model including pressure perturbations. *Monthly Weather Review*, *101*(3), 201-205. Retrieved from https://doi.org/10.1175/1520-0493(1973)101<0201:AOCMIP>2.3.CO;2 doi: 10.1175/1520-0493(1973)101⟨0201:AOCMIP⟩2.3.CO;2

Houze, R. A. (2004). Mesoscale convective systems. *Rev. Geophys.*, *42*(RG4003). doi: 10.1029/2004RG000150

Houze, R. A., Jr. (2018). 100 years of research on mesoscale convective systems. *Meteorological Monographs*, *59*, 17.1-17.54. doi: 10.1175/AMSMONOGRAPHS-D-18-0001.1

Jensen, M. P., Ackerman, T. P., & Sekelsky, S. M. (2002). Radiative impacts of anvil cloud during the maritime continent thunderstorm experiment. *Journal of Applied Meteorology*, *41*(5), 473-487. Retrieved from https://doi.org/10.1175/1520-0450(2002)041<0473:RIOACD>2.0.CO;2 doi: 10.1175/1520-0450(2002)041⟨0473:RIOACD⟩2.0.CO;2

Jensen, M. P., & Del Genio, A. D. (2003). Radiative and microphysical characteristics of deep convective systems in the tropical western pacific. *Journal of Applied Meteorology*, *42*(9), 1234-1254. Retrieved from https://doi.org/10.1175/1520-0450(2003)042<1234:RAMCOD>2.0.CO;2 doi: 10.1175/1520-0450(2003)042⟨1234:RAMCOD⟩2.0.CO;2

Jensen, M. P., & Del Genio, A. D. (2006). Factors limiting convective cloud-top height at the arm nauru island climate research facility. *Journal of Climate*, *19*(10), 2105-2117. doi: 10.1175/JCLI3722.1

Jensen, M. P., Mather, J. H., & Ackerman, T. P. (1998). Observations of the 1997–98 warm enso event at the manus island arm site. *Geophysical Research Letters*, *25*(24), 4517-4520. Retrieved from https://agupubs.onlinelibrary.wiley.com/doi/abs/10.1029/1998GL900185 doi: 10.1029/1998GL900185

Jensen, M. P., Toto, T., Troyan, D., Ciesielski, P. E., Holdridge, D., Kyrouac, J., ... Xie, S. (2015). The midlatitude continental convective clouds experiment (mc3e) sounding network: operations, processing and analysis. *Atmospheric Measurement Techniques*, *8*(1), 421–434. doi: 10.5194/amt-8-421-2015

Jorgensen, D. P., & LeMone, M. A. (1989). Vertical velocity characteristics of oceanic convection. *Journal of the Atmospheric Sciences*, *46*(5), 621-640. Retrieved from https://doi.org/10.1175/1520-0469(1989)046<0621:VVCOOC>2.0.CO;2 doi: 10.1175/1520-0469(1989)046⟨0621:VVCOOC⟩2.0.CO;2

Kain, J. S., & Fritsch, J. M. (1990). A one-dimensional entraining/detraining plume model and its application in convective parameterization. *Journal of the Atmospheric Sciences*, *47*(23), 2784-2802. Retrieved from

https://doi.org/10.1175/1520-0469(1990)047<2784:AODEPM>2.0.CO;2 doi: 10.1175/1520-0469(1990)047⟨2784:AODEPM⟩2.0.CO;2

Keenan, T. D., & Carbone, R. E. (1992). A preliminary morphology of precipitation systems in tropical northern australia. *Quarterly Journal of the Royal Meteorological Society*, *118*(504), 283-326. Retrieved from https://rmets.onlinelibrary.wiley.com/doi/abs/10.1002/qj.49711850406 doi: 10.1002/qj.49711850406

Khairoutdinov, M., & Randall, D. (2006, Dec). High-Resolution Simulation of Shallow-to-Deep Convection Transition over Land. *Journal of Atmospheric Sciences*, *63*(12), 3421-3436. doi: 10.1175/JAS3810.1

Kim, D., & Kang, I. (2012). A bulk mass flux convection scheme for climate model: description and moisture sensitivity. *Clim Dyn*, *38*, 411–429. Retrieved from https://doi.org/10.1007/s00382-010-0972-2 doi: 10.1007/s00382-010-0972-2

Kirkpatrick, C., McCaul, E. W., & Cohen, C. (2009). Variability of updraft and downdraft characteristics in a large parameter space study of convective storms. *Monthly Weather Review*, *137*(5), 1550-1561. Retrieved from https://doi.org/10.1175/2008MWR2703.1 doi: 10.1175/2008MWR2703.1

Klocke, D., Pincus, R., & Quaas, J. (2011). On constraining estimates of climate sensitivity with present-day observations through model weighting. *Journal of Climate*, *24*(23), 6092-6099. Retrieved from https://doi.org/10.1175/2011JCLI4193.1 doi: 10.1175/2011JCLI4193.1

Kollias, P., Albrecht, B. A., Clothiaux, E. E., Miller, M. A., Johnson, K. L., & Moran, K. P. (2005). The atmospheric radiation measurement program cloud profiling radars: An evaluation of signal processing and sampling strategies. *Journal of Atmospheric and Oceanic Technology*, *22*(7), 930-948. Retrieved from https://doi.org/10.1175/JTECH1749.1 doi: 10.1175/JTECH1749.1

Kollias, P., Miller, M. A., Johnson, K. L., Jensen, M. P., & Troyan, D. T. (2009). Cloud, thermodynamic, and precipitation observations in west africa during 2006. *Journal of Geophysical Research: Atmospheres*, *114*(D13). Retrieved from https://agupubs.onlinelibrary.wiley.com/doi/abs/10.1029/2008JD010641 doi: 10.1029/2008JD010641

Kollias, P., Miller, M. A., Luke, E. P., Johnson, K. L., Clothiaux, E. E., Moran,

K. P., ... Albrecht, B. A. (2007). The atmospheric radiation measurement program cloud profiling radars: Second-generation sampling strategies, processing, and cloud data products. *Journal of Atmospheric and Oceanic Technology*, *24*(7), 1199-1214. Retrieved from https://doi.org/10.1175/JTECH2033.1 doi: 10.1175/JTECH2033.1

Kuang, Z., & Bretherton, C. S. (2006). A mass-flux scheme view of a high-resolution simulation of a transition from shallow to deep cumulus convection. *Journal of the Atmospheric Sciences*, *63*(7), 1895-1909. Retrieved from https://doi.org/10.1175/JAS3723.1 doi: 10.1175/JAS3723.1

Lebel, T., Diedhiou, A., & Laurent, H. (2003). Seasonal cycle and interannual variability of the sahelian rainfall at hydrological scales. *Journal of Geophysical Research: Atmospheres*, *108*(D8). Retrieved from https://agupubs.onlinelibrary.wiley.com/doi/abs/10.1029/2001JD001580 doi: 10.1029/2001JD001580

Liaw, A., & Wiener, M. (2002). Classification and Regression by randomForest. *R News*, *2*(3), 18–22. Retrieved from http://CRAN.R-project.org/doc/Rnews/

Long, C. (2010). *Amie (arm mjo investigation experiment): Observations of the madden-julian oscillation for modeling studies science plan.* (Tech. Rep. No. DOE/SC-ARM-10-007). DOE ARM Climate Research Facility.

Long, C. (2011). *Arm mjo investigation experiment on gan island (amie-gan) science plan.* (Tech. Rep. No. DOE/SC-ARM-11-005). DOE ARM Climate Research Facility.

Long, C., Mather, J. H., & Ackerman, T. P. (2016). The arm tropical western pacific (twp) sites. *Meteorological Monographs*, *57*, 7.1-7.14. Retrieved from https://doi.org/10.1175/AMSMONOGRAPHS-D-15-0024.1 doi: 10.1175/AMSMONOGRAPHS-D-15-0024.1

Long, C., McFarlane, S. A., Genio, A. D., Minnis, P., Ackerman, T. P., Mather, J., ... Jakob, C. (2013). Arm research in the equatorial western pacific: A decade and counting. *Bulletin of the American Meteorological Society*, *94*(5), 695-708. Retrieved from https://doi.org/10.1175/BAMS-D-11-00137.1 doi: 10.1175/BAMS-D-11-00137.1

Lu, C.-S., LIU, Y.-G., NIU, S.-J., & XUE, Y.-Q. (2018). Broadening of cloud

droplet size distributions and warm rain initiation associated with turbulence: an overview. *Atmospheric and Oceanic Science Letters*, *11*(2), 123-135. Retrieved from https://doi.org/10.1080/16742834.2018.1410057 doi: 10.1080/16742834.2018.1410057

Lucas, C., Zipser, E. J., & LeMone, M. A. (1994a). Convective available potential energy in the environment of oceanic and continental clouds: Correction and comments. *Journal of the Atmospheric Sciences*, *51*(24), 3829-3830. doi: 10.1175/1520-0469(1994)051⟨3829:CAPEIT⟩2.0.CO;2

Lucas, C., Zipser, E. J., & LeMone, M. A. (1994b). Vertical velocity in oceanic convection off tropical australia. *Journal of the Atmospheric Sciences*, *51*(21), 3183-3193. doi: 10.1175/1520-0469(1994)051⟨3183:VVIOCO⟩2.0.CO;2

Machado, L. A. T., Calheiros, A. J. P., Biscaro, T., Giangrande, S., Silva Dias, M. A. F., Cecchini, M. A., ... Wendisch, M. (2018). Overview: Precipitation characteristics and sensitivities to environmental conditions during goamazon2014/5 and acridicon-chuva. *Atmospheric Chemistry and Physics*, *18*(9), 6461–6482. Retrieved from https://www.atmos-chem-phys.net/18/6461/2018/ doi: 10.5194/acp-18-6461-2018

Maloney, E. D., & Hartmann, D. L. (2001). The sensitivity of intraseasonal variability in the ncar ccm3 to changes in convective parameterization. *Journal of Climate*, *14*(9), 2015-2034. Retrieved from https://doi.org/10.1175/1520-0442(2001)014<2015:TSOIVI>2.0.CO;2 doi: 10.1175/1520-0442(2001)014⟨2015:TSOIVI⟩2.0.CO;2

Martin, S. T., Artaxo, P., Machado, L. A. T., Manzi, A. O., Souza, R. A. F., Schumacher, C., ... Wendisch, M. (2016). Introduction: Observations and modeling of the green ocean amazon (goamazon2014/5). *Atmospheric Chemistry and Physics*, *16*(8), 4785-4797. doi: 10.5194/acp-16-4785-2016

Mather, J. H., Ackerman, T. P., Jensen, M. P., & Clements, W. E. (1998). Characteristics of the atmospheric state and the surface radiation budget at the tropical western pacific arm site. *Geophysical Research Letters*, *25*(24), 4513-4516. Retrieved from https://agupubs.onlinelibrary.wiley.com/doi/abs/10.1029/1998GL900196 doi: 10.1029/1998GL900196

Mather, J. H., & Voyles, J. W. (2013). The arm climate research facility: A review of structure and capabilities. *Bulletin of the American Meteorological Society*,

94(3), 377-392. doi: 10.1175/BAMS-D-11-00218.1

May, P. T., Long, C. N., & Protat, A. (2012). The diurnal cycle of the boundary layer, convection, clouds, and surface radiation in a coastal monsoon environment (darwin, australia). *Journal of Climate*, *25*(15), 5309-5326. Retrieved from https://doi.org/10.1175/JCLI-D-11-00538.1 doi: 10.1175/JCLI-D-11-00538.1

May, R. M., Arms, S. C., Marsh, P., Bruning, E., Leeman, J. R., Goebbert, K., ... Bruick, Z. S. (2008 - 2020). Metpy: A Python package for meteorological data. Retrieved from https://github.com/Unidata/MetPy doi: 10.5065/D6WW7G29

McCaul, E. W., & Weisman, M. L. (2001). The sensitivity of simulated supercell structure and intensity to variations in the shapes of environmental buoyancy and shear profiles. *Monthly Weather Review*, *129*(4), 664-687. Retrieved from https://doi.org/10.1175/1520-0493(2001)129<0664:TSOSSS>2.0.CO;2 doi: 10.1175/1520-0493(2001)129⟨0664:TSOSSS⟩2.0.CO;2

McFarlane, S. A., Long, C. N., & Flaherty, J. (2013). A climatology of surface cloud radiative effects at the arm tropical western pacific sites. *Journal of Applied Meteorology and Climatology*, *52*(4), 996-1013. Retrieved from https://doi.org/10.1175/JAMC-D-12-0189.1 doi: 10.1175/JAMC-D-12-0189.1

Mera, R., Laing, A. G., & Semazzi, F. (2014). Moisture variability and multiscale interactions during spring in west africa. *Monthly Weather Review*, *142*(9), 3178-3198. Retrieved from https://doi.org/10.1175/MWR-D-13-00175.1 doi: 10.1175/MWR-D-13-00175.1

Miller, M. A., Nitschke, K., Ackerman, T. P., Ferrell, W., Hickmon, N., & Ivey, M. (2016). The atmospheric radiation measurement mobile facility, the atmospheric radiation measurement (arm) program: Ams monograph, the first 20 years of arm. *Am. Meteorol. Soc.*. doi: 10.1175/AMSMONOGRAPHS-D-15-0051.1

Miller, M. A., & Slingo, A. (2007). The arm mobile facility and its first international deployment: Measuring radiative flux divergence in west africa. *Bulletin of the American Meteorological Society*, *88*(8), 1229-1244. Retrieved from https://doi.org/10.1175/BAMS-88-8-1229 doi: 10.1175/BAMS-88-8-1229

Mullendore, G. L., Durran, D. R., & Holton, J. R. (2005). Cross-tropopause tracer

transport in midlatitude convection. *Journal of Geophysical Research: Atmospheres*, *110*(D6). Retrieved from https://agupubs.onlinelibrary.wiley.com/doi/abs/10.1029/2004JD005059 doi: 10.1029/2004JD005059

Mullendore, G. L., Homann, A. J., Bevers, K., & Schumacher, C. (2009). Radar reflectivity as a proxy for convective mass transport. *Journal of Geophysical Research: Atmospheres*, *114*(D16). Retrieved from https://agupubs.onlinelibrary.wiley.com/doi/abs/10.1029/2008JD011431 doi: 10.1029/2008JD011431

Mullendore, G. L., Homann, A. J., Jorgenson, S. T., Lang, T. J., & Tessendorf, S. A. (2013). Relationship between level of neutral buoyancy and dual-doppler observed mass detrainment levels in deep convection. *Atmospheric Chemistry and Physics*, *13*(1), 181–190. Retrieved from https://www.atmos-chem-phys.net/13/181/2013/ doi: 10.5194/acp-13-181-2013

Norgren, M. S., Small, J. D., Jonsson, H. H., & Chuang, P. Y. (2016). Observational estimates of detrainment and entrainment in non-precipitating shallow cumulus. *Atmospheric Chemistry and Physics*, *16*(1), 21–33. Retrieved from https://www.atmos-chem-phys.net/16/21/2016/ doi: 10.5194/acp-16-21-2016

Pedregosa, F., Varoquaux, G., Gramfort, A., Michel, V., Thirion, B., Grisel, O., ... Duchesnay, E. (2011). Scikit-learn: Machine learning in Python. *Journal of Machine Learning Research*, *12*, 2825–2830.

Peters, J. M., Hannah, W., & Morrison, H. (2019). The influence of vertical wind shear on moist thermals. *Journal of the Atmospheric Sciences*, *76*(6), 1645-1659. Retrieved from https://doi.org/10.1175/JAS-D-18-0296.1 doi: 10.1175/JAS-D-18-0296.1

Pope, M., Jakob, C., & Reeder, M. J. (2009). Regimes of the north australian wet season. *Journal of Climate*, *22*(24), 6699-6715. Retrieved from https://doi.org/10.1175/2009JCLI3057.1 doi: 10.1175/2009JCLI3057.1

Pope, S. B. (2000). *Turbulent flows*. Cambridge University Press.

Porch, W. M., Olsen, S. C., Chylek, P., Dubey, M. K., Henderson, B. G., & Clodius, W. (2006). Satellite and surface observations of nauru island clouds: Differences between el nino and la nina periods. *Geophysical Research Letters*, *33*(13). Retrieved from https://agupubs.onlinelibrary.wiley.com/doi/

abs/10.1029/2006GL026339 doi: 10.1029/2006GL026339

Quinlan, J. R. (1993). *C4.5: Programs for machine learning*. San Francisco, CA, USA: Morgan Kaufmann Publishers Inc.

Raga, G. B., Jensen, J. B., & Baker, M. B. (1990). Characteristics of cumulus band clouds off the coast of hawaii. *Journal of the Atmospheric Sciences*, *47*(3), 338-356. Retrieved from https://doi.org/10.1175/1520-0469(1990)047<0338:COCBCO>2.0.CO;2 doi: 10.1175/1520-0469(1990)047⟨0338:COCBCO⟩2.0.CO;2

Ritsche, M. (2011). *Arm surface meteorology systems handbook* (Tech. Rep. No. DOE/SC-ARM/TR-086). U.S. Department of Energy.

Romps, D. M. (2010). A direct measure of entrainment. *Journal of the Atmospheric Sciences*, *67*(6), 1908-1927. Retrieved from https://doi.org/10.1175/2010JAS3371.1 doi: 10.1175/2010JAS3371.1

Romps, D. M., & Charn, A. B. (2015). Sticky thermals: Evidence for a dominant balance between buoyancy and drag in cloud updrafts. *Journal of the Atmospheric Sciences*, *72*(8), 2890-2901. Retrieved from https://doi.org/10.1175/JAS-D-15-0042.1 doi: 10.1175/JAS-D-15-0042.1

Sanderson, B. M., Piani, C., Ingram, W. J., Stone, D. A., & Allen, M. R. (2008, Feb 01). Towards constraining climate sensitivity by linear analysis of feedback patterns in thousands of perturbed-physics gcm simulations. *Climate Dynamics*, *30*(2), 175–190. doi: 10.1007/s00382-007-0280-7

Schiro, K. A., & Neelin, J. D. (2018). Tropical continental downdraft characteristics: mesoscale systems versus unorganized convection. *Atmospheric Chemistry and Physics*, *18*(3), 1997–2010. doi: 10.5194/acp-18-1997-2018

Schiro, K. A., & Neelin, J. D. (2019). Deep convective organization, moisture vertical structure, and convective transition using deep-inflow mixing. *Journal of the Atmospheric Sciences*, *76*(4), 965-987. Retrieved from https://doi.org/10.1175/JAS-D-18-0122.1 doi: 10.1175/JAS-D-18-0122.1

Schiro, K. A., Neelin, J. D., Adams, D. K., & Lintner, B. R. (2016). Deep convection and column water vapor over tropical land versus tropical ocean: A comparison between the amazon and the tropical western pacific. *Journal of the Atmospheric Sciences*, *73*(10), 4043-4063. Retrieved from https://doi.org/10.1175/JAS-D-16-0119.1 doi: 10.1175/JAS-D-16-0119.1

Seibert, P., Beyrich, F., Gryning, S.-E., Joffre, S., Rasmussen, A., & Tercier, P. (2000). Review and intercomparison of operational methods for the determination of the mixing height. *Atmospheric Environment*, *34*(7), 1001 - 1027. Retrieved from http://www.sciencedirect.com/science/article/pii/S1352231099003490 doi: https://doi.org/10.1016/S1352-2310(99)00349-0

Sherwood, S. C., Hernández-Deckers, D., Colin, M., & Robinson, F. (2013). Slippery thermals and the cumulus entrainment paradox. *Journal of the Atmospheric Sciences*, *70*(8), 2426-2442. Retrieved from https://doi.org/10.1175/JAS-D-12-0220.1 doi: 10.1175/JAS-D-12-0220.1

Sivaraman, C., McFarlane, S., Chapman, E., Jensen, M., Toto, T., Liu, S., & Fischer, M. (2013). *Planetary boundary layer height (pbl) value added product (vap): Radiosonde retrievals.* (Tech. Rep. No. DOE/SC-ARM/TR-132). U.S. DOE, Office of Science, Office of Biological and Environmental Research.

Slingo, A., Bharmal, N. A., Robinson, G. J., Settle, J. J., Allan, R. P., White, H. E., ... Miller, M. (2008). Overview of observations from the radagast experiment in niamey, niger: Meteorology and thermodynamic variables. *Journal of Geophysical Research: Atmospheres*, *113*(D13). Retrieved from https://agupubs.onlinelibrary.wiley.com/doi/abs/10.1029/2008JD009909 doi: 10.1029/2008JD009909

Stanfield, R. E., Su, H., Jiang, J. H., Freitas, S. R., Molod, A. M., Luo, Z. J., ... Luo, M. (2019). Convective entrainment rates estimated from aura co and cloudsat/calipso observations and comparison with geos-5. *Journal of Geophysical Research: Atmospheres*, *124*(17-18), 9796-9807. Retrieved from https://agupubs.onlinelibrary.wiley.com/doi/abs/10.1029/2019JD030846 doi: 10.1029/2019JD030846

Stephens, G. L. (2005). Cloud feedbacks in the climate system: A critical review. *Journal of Climate*, *18*(2), 237-273. Retrieved from https://doi.org/10.1175/JCLI-3243.1 doi: 10.1175/JCLI-3243.1

Stirling, A. J., & Stratton, R. A. (2012). Entrainment processes in the diurnal cycle of deep convection over land. *Quarterly Journal of the Royal Meteorological Society*, *138*(666), 1135-1149. Retrieved from https://rmets.onlinelibrary.wiley.com/doi/abs/10.1002/qj.1868 doi: 10.1002/qj.1868

Stokes, G. M., & Schwartz, S. E. (1994). The atmospheric radiation measurement

(arm) program: Programmatic background and design of the cloud and radiation test bed. *Bulletin of the American Meteorological Society*, *75*(7), 1201-1222. Retrieved from https://doi.org/10.1175/1520-0477(1994)075<1201:TARMPP>2.0.CO;2 doi: 10.1175/1520-0477(1994)075⟨1201:TARMPP⟩2.0.CO;2

Stommel, H. (1947). Entrainment of air into a cumulus cloud. *Journal of Meteorology*, *4*(3), 91-94. Retrieved from https://doi.org/10.1175/1520-0469(1947)004<0091:EOAIAC>2.0.CO;2 doi: 10.1175/1520-0469(1947)004⟨0091:EOAIAC⟩2.0.CO;2

Takahashi, H., & Luo, Z. (2012). Where is the level of neutral buoyancy for deep convection? *Geophysical Research Letters*, *39*(15). Retrieved from https://agupubs.onlinelibrary.wiley.com/doi/abs/10.1029/2012GL052638 doi: 10.1029/2012GL052638

Takahashi, H., Luo, Z. J., & Stephens, G. L. (2017). Level of neutral buoyancy, deep convective outflow, and convective core: New perspectives based on 5 years of cloudsat data. *Journal of Geophysical Research: Atmospheres*, *122*(5), 2958-2969. Retrieved from https://agupubs.onlinelibrary.wiley.com/doi/abs/10.1002/2016JD025969 doi: 10.1002/2016JD025969

Tanelli, S., Durden, S. L., Im, E., Pak, K. S., Reinke, D. G., Partain, P., ... Marchand, R. T. (2008, Nov). Cloudsat's cloud profiling radar after two years in orbit: Performance, calibration, and processing. *IEEE Transactions on Geoscience and Remote Sensing*, *46*(11), 3560-3573. doi: 10.1109/TGRS.2008.2002030

Tokioka, T., Yamazaki, K., Kitoh, A., & Ose, T. (1988). The equatorial 30-60 day oscillation and the arakawa-schubert penetrative cumulus parameterization. *Journal of the Meteorological Society of Japan. Ser. II*, *66*(6), 883-901. doi: 10.2151/jmsj1965.66.6_883

Wang, D., Giangrande, S. E., Bartholomew, M. J., Hardin, J., Feng, Z., Thalman, R., & Machado, L. A. T. (2018). The green ocean: precipitation insights from the goamazon2014/5 experiment. *Atmospheric Chemistry and Physics*, *18*(12), 9121–9145. doi: 10.5194/acp-18-9121-2018

Wang, D., Giangrande, S. E., Schiro, K. A., Jensen, M. P., & Houze, R. A. J. (2019). The characteristics of tropical and midlatitude mesoscale convective

systems as revealed by radar wind profilers. *Journal of Geophysical Research: Atmospheres*, *124*, 1-19. doi: 10.1029/2018JD030087

Weisman, M. L., & Klemp, J. B. (1984). The structure and classification of numerically simulated convective stormsin directionally varying wind shears. *Monthly Weather Review*, *112*(12), 2479-2498. Retrieved from https://doi.org/10.1175/1520-0493(1984)112<2479:TSACON>2.0.CO;2 doi: 10.1175/1520-0493(1984)112⟨2479:TSACON⟩2.0.CO;2

Widener, K., Bharadwaj, N., & Johnson, K. (2012). *Ka-band arm zenith radar handbook* (Tech. Rep. No. DOE/SC-ARM/TR-106). U.S. Department of Energy.

Widener, K., & Mead, J. (Eds.). (2004, March). *W-band arm cloud radar—specifications and design.* Albuquerque, New Mexico.

Yang, G.-Y., & Slingo, J. (2001). The diurnal cycle in the tropics. *Monthly Weather Review*, *129*(4), 784-801. Retrieved from https://doi.org/10.1175/1520-0493(2001)129<0784:TDCITT>2.0.CO;2 doi: 10.1175/1520-0493(2001)129⟨0784:TDCITT⟩2.0.CO;2

Yoneyama, K., Zhang, C., & Long, C. N. (2013). Tracking pulses of the madden–julian oscillation. *Bulletin of the American Meteorological Society*, *94*(12), 1871-1891. Retrieved from https://doi.org/10.1175/BAMS-D-12-00157.1 doi: 10.1175/BAMS-D-12-00157.1

Zhang, G., & McFarlane, N. A. (1995). Sensitivity of climate simulations to the parameterization of cumulus convection in the canadian climate centre general circulation model. *Atmosphere-Ocean*, *33*(3), 407-446. Retrieved from https://doi.org/10.1080/07055900.1995.9649539 doi: 10.1080/07055900.1995.9649539

Zipser, E. J. (2003). Some views on "hot towers" after 50 years of tropical field programs and two years of trmm data. *Meteorological Monographs*, *51*, 49-58. doi: 10.1175/0065-9401(2003)029⟨0049:CSVOHT⟩2.0.CO;2

Figure 1.

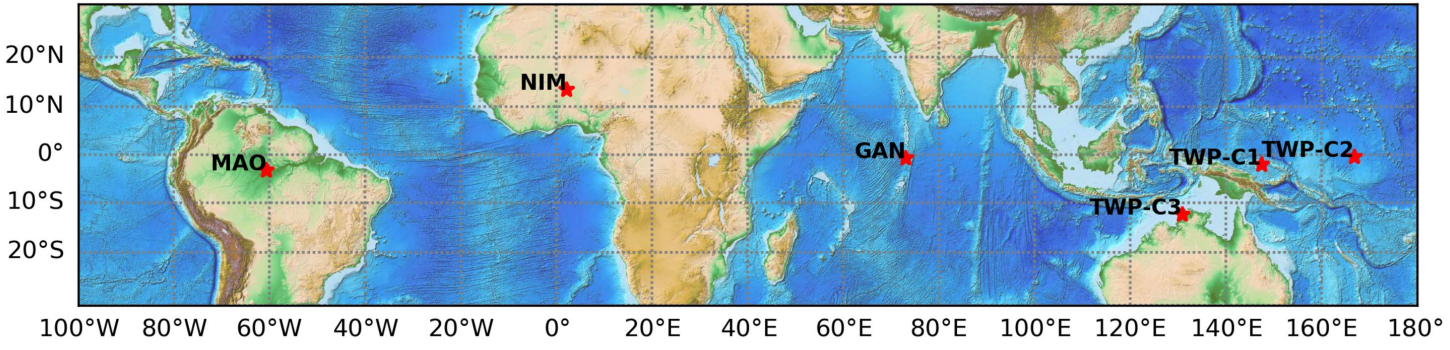

Figure 2.

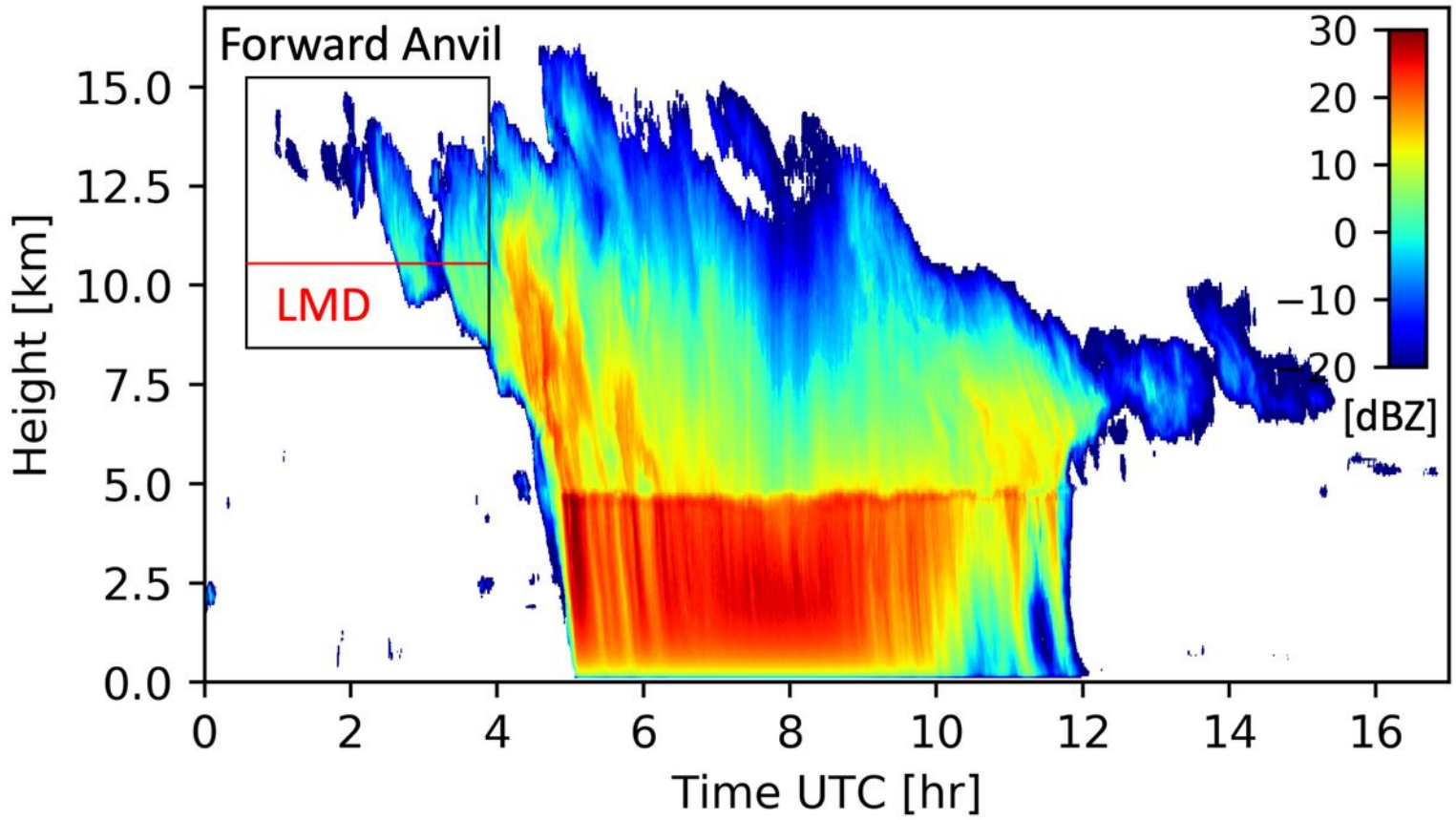
Forward Anvil
LMD
Height [km]
15.0
12.5
10.0
7.5
5.0
2.5
0.0
0
2
4
6
8
10
12
14
16
Time UTC [hr]
30
20
10
0
−10
−20
[dBZ]

Figure 3.

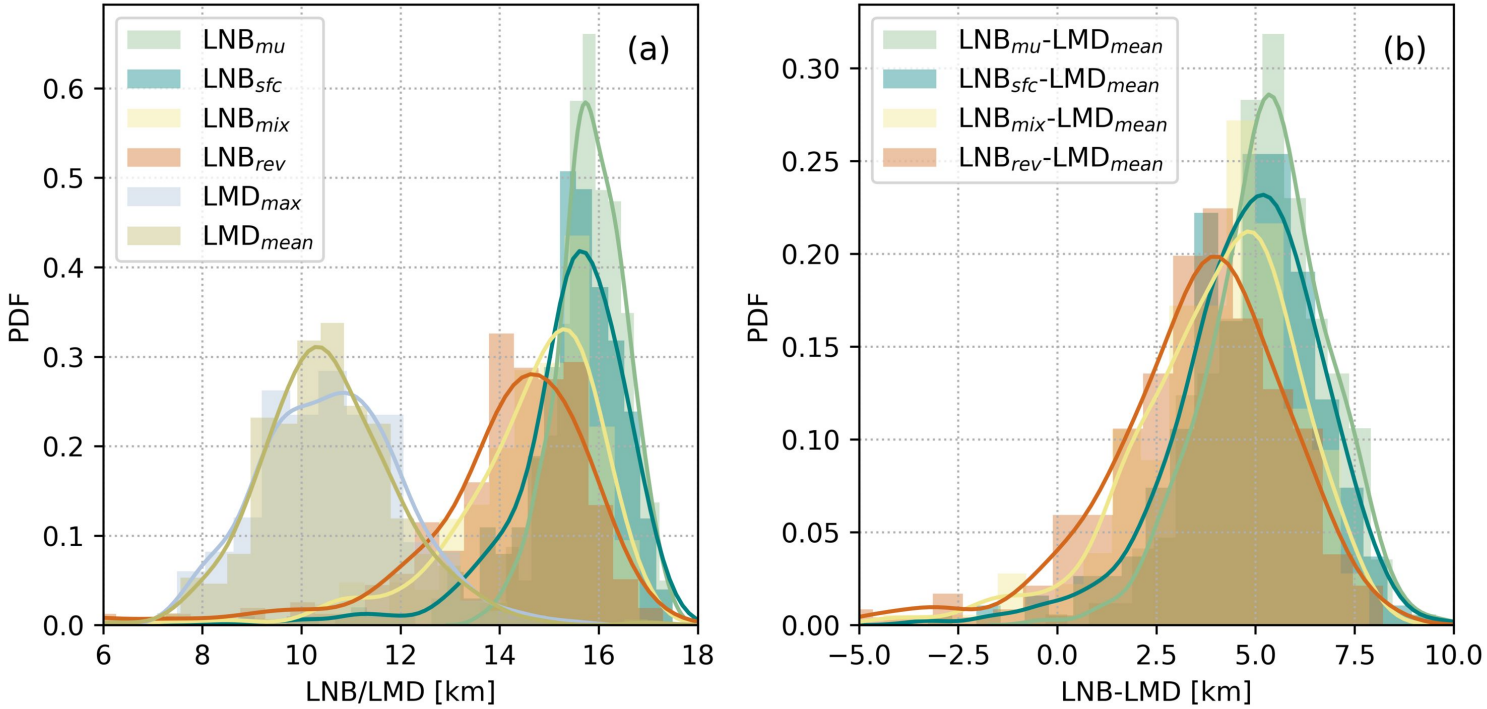
(a)
LNB$_{mu}$
LNB$_{sfc}$
LNB$_{mix}$
LNB$_{rev}$
LMD$_{max}$
LMD$_{mean}$
PDF
LNB/LMD [km]
(b)
LNB$_{mu}$-LMD$_{mean}$
LNB$_{sfc}$-LMD$_{mean}$
LNB$_{mix}$-LMD$_{mean}$
LNB$_{rev}$-LMD$_{mean}$
PDF
LNB-LMD [km]

Figure 4.

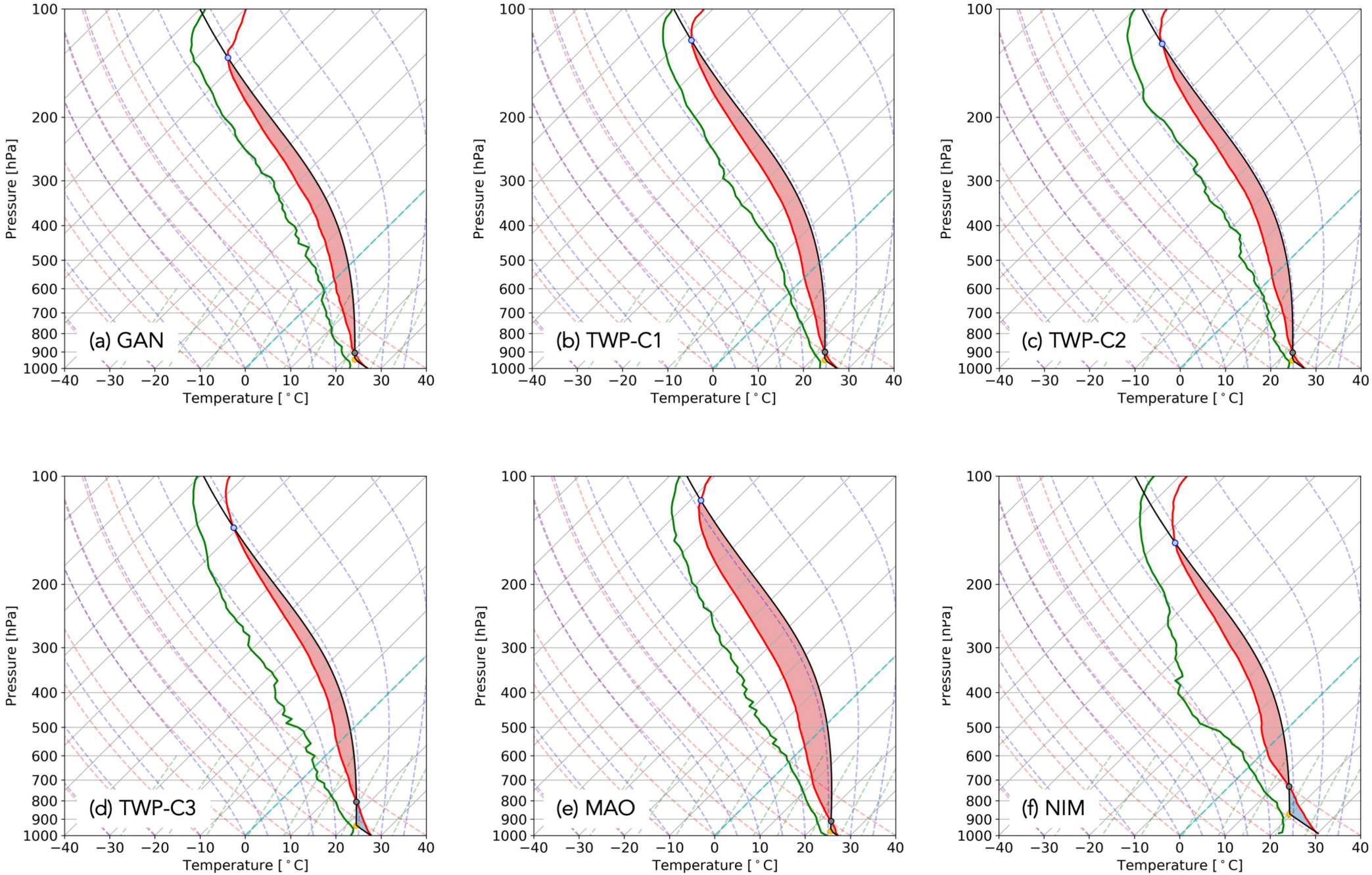
(a) GAN
(b) TWP-C1
(c) TWP-C2
(d) TWP-C3
(e) MAO
(f) NIM
Pressure [hPa]
Temperature [° C]
100
200
300
400
500
600
700
800
900
1000
−40
−30
−20
−10
0
10
20
30
40

Figure 5.

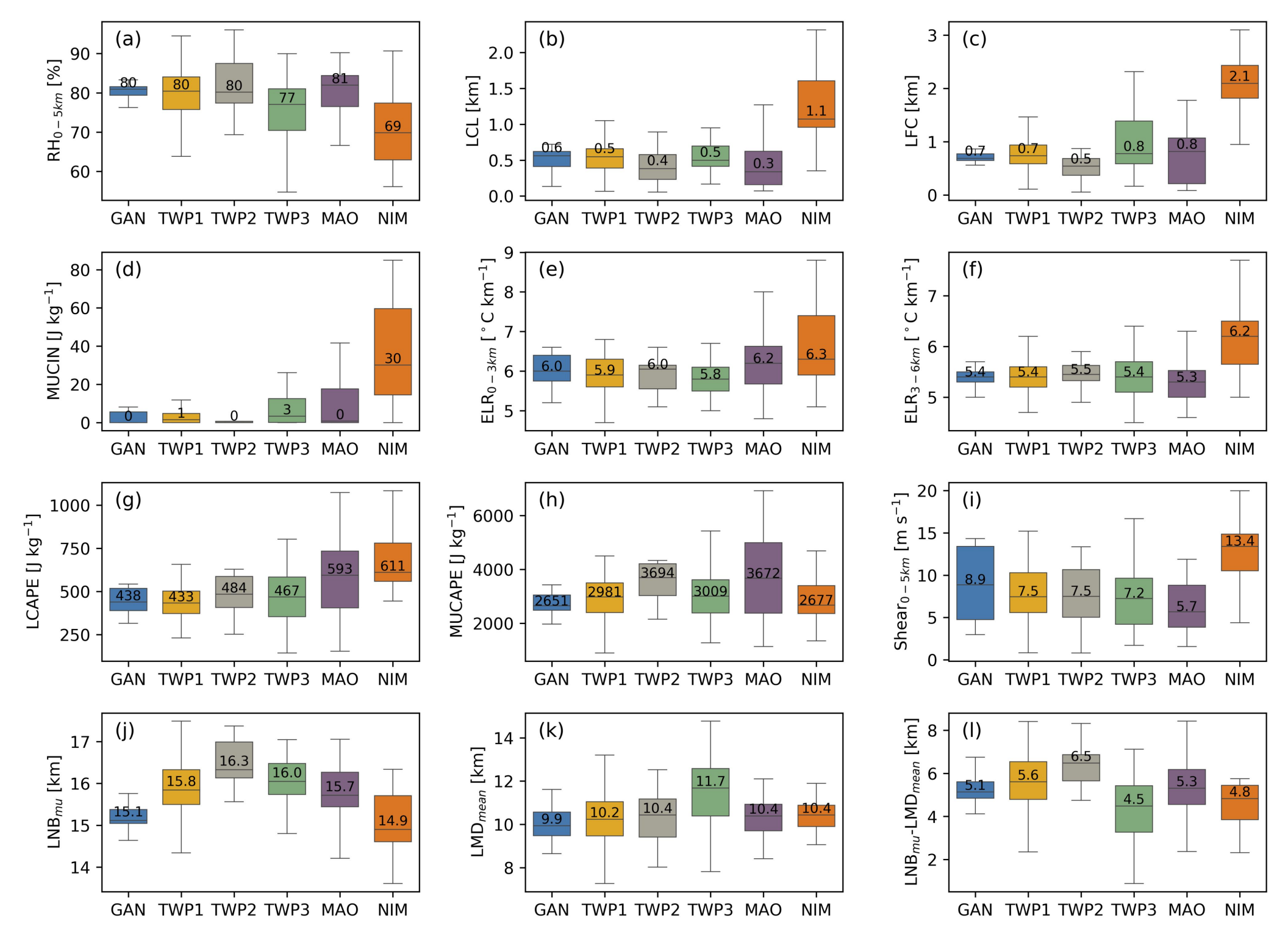
(a)
RH_{0-5km} [%]
80
80
80
77
81
69
(b)
LCL [km]
0.6
0.5
0.4
0.5
0.3
1.1
(c)
LFC [km]
0.7
0.7
0.5
0.8
0.8
2.1
(d)
MUCIN [J kg^{-1}]
0
1
0
3
0
30
(e)
ELR_{0-3km} [$^{\circ}$C km^{-1}]
6.0
5.9
6.0
5.8
6.2
6.3
(f)
ELR_{3-6km} [$^{\circ}$C km^{-1}]
5.4
5.4
5.5
5.4
5.3
6.2
(g)
LCAPE [J kg^{-1}]
438
433
484
467
593
611
(h)
MUCAPE [J kg^{-1}]
2651
2981
3694
3009
3672
2677
(i)
$Shear_{0-5km}$ [m s^{-1}]
8.9
7.5
7.5
7.2
5.7
13.4
(j)
LNB_{mu} [km]
15.1
15.8
16.3
16.0
15.7
14.9
(k)
LMD_{mean} [km]
9.9
10.2
10.4
11.7
10.4
10.4
(l)
LNB_{mu}-LMD_{mean} [km]
5.1
5.6
6.5
4.5
5.3
4.8
GAN
TWP1
TWP2
TWP3
MAO
NIM

Figure 6.

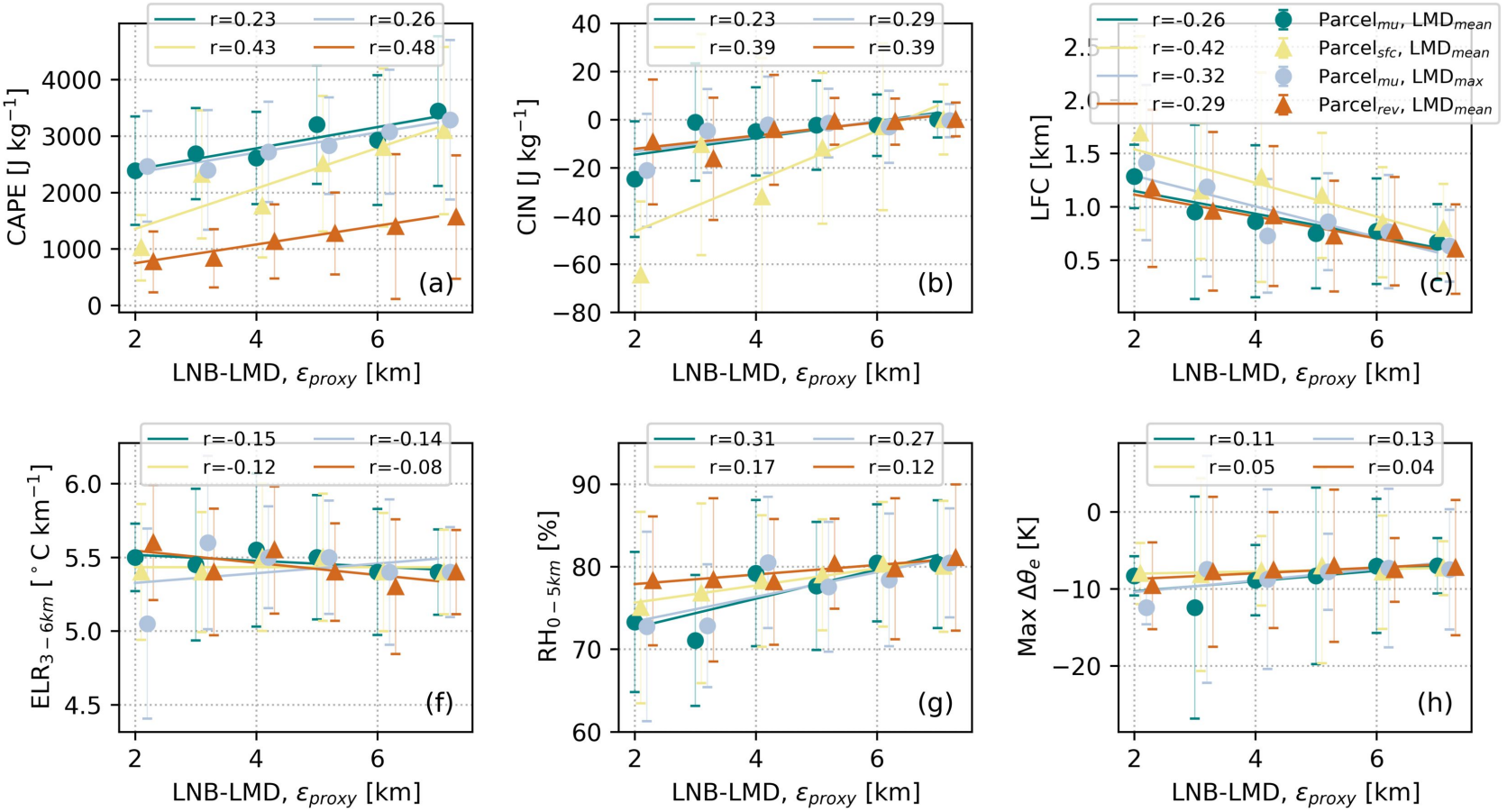
r=0.23
r=0.26
r=0.43
r=0.48
CAPE [J kg^{-1}]
(a)
LNB-LMD, ε_{proxy} [km]
r=0.23
r=0.29
r=0.39
r=0.39
CIN [J kg^{-1}]
(b)
LNB-LMD, ε_{proxy} [km]
r=-0.26
r=-0.42
r=-0.32
r=-0.29
Parcel$_{mu}$, LMD$_{mean}$
Parcel$_{sfc}$, LMD$_{mean}$
Parcel$_{mu}$, LMD$_{max}$
Parcel$_{rev}$, LMD$_{mean}$
LFC [km]
(c)
LNB-LMD, ε_{proxy} [km]
r=-0.15
r=-0.14
r=-0.12
r=-0.08
ELR$_{3-6km}$ [$^\circ$C km^{-1}]
(f)
LNB-LMD, ε_{proxy} [km]
r=0.31
r=0.27
r=0.17
r=0.12
RH$_{0-5km}$ [%]
(g)
LNB-LMD, ε_{proxy} [km]
r=0.11
r=0.13
r=0.05
r=0.04
Max $\Delta\theta_e$ [K]
(h)
LNB-LMD, ε_{proxy} [km]

Figure 7.

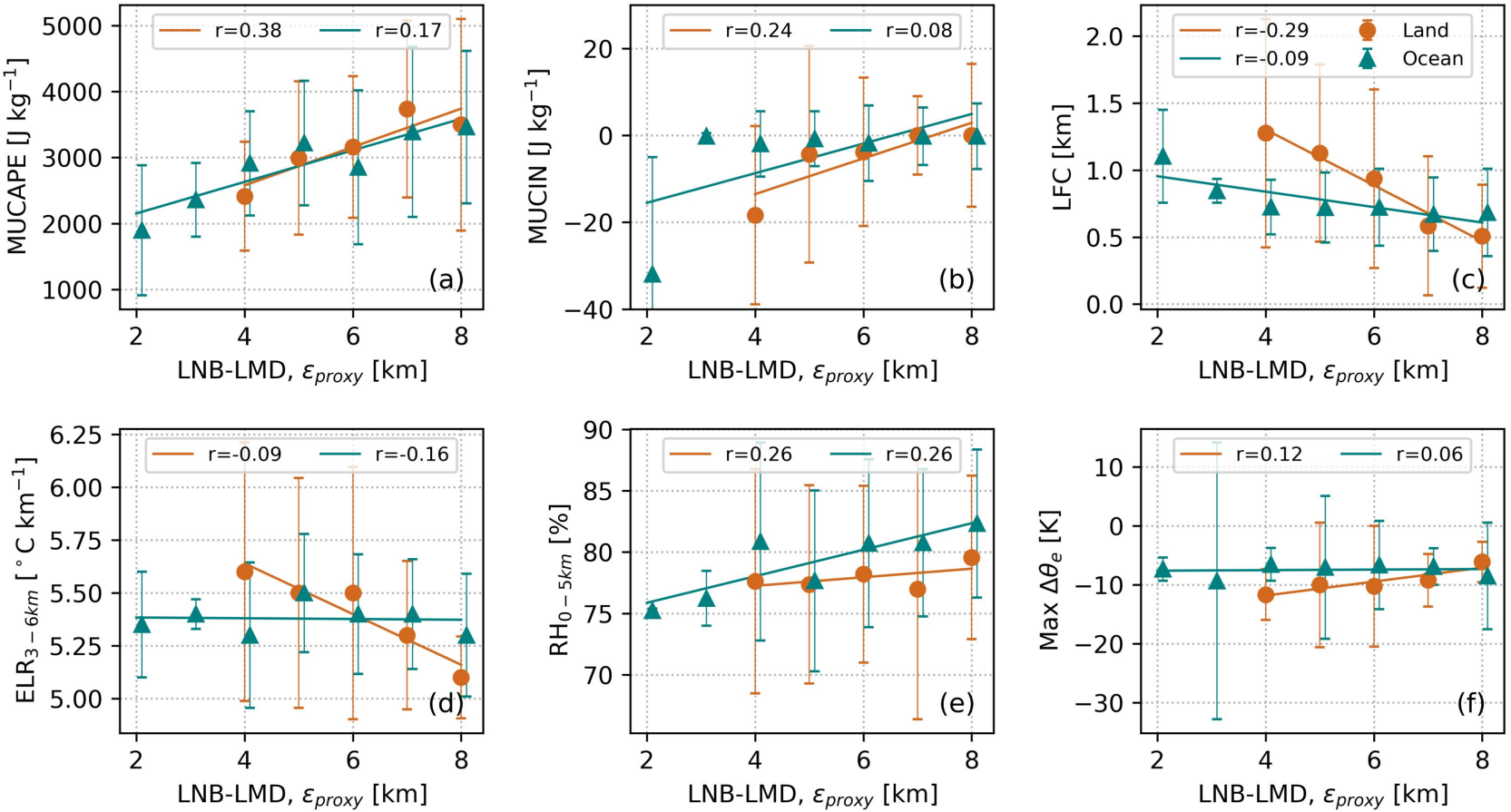
r=0.38
r=0.17
MUCAPE [J kg^{-1}]
(a)
LNB-LMD, ε_{proxy} [km]
r=0.24
r=0.08
MUCIN [J kg^{-1}]
(b)
LNB-LMD, ε_{proxy} [km]
r=-0.29
r=-0.09
Land
Ocean
LFC [km]
(c)
LNB-LMD, ε_{proxy} [km]
r=-0.09
r=-0.16
ELR_{3-6km} [$^\circ$C km^{-1}]
(d)
LNB-LMD, ε_{proxy} [km]
r=0.26
r=0.26
RH_{0-5km} [%]
(e)
LNB-LMD, ε_{proxy} [km]
r=0.12
r=0.06
Max $\Delta\theta_e$ [K]
(f)
LNB-LMD, ε_{proxy} [km]

Figure 8.

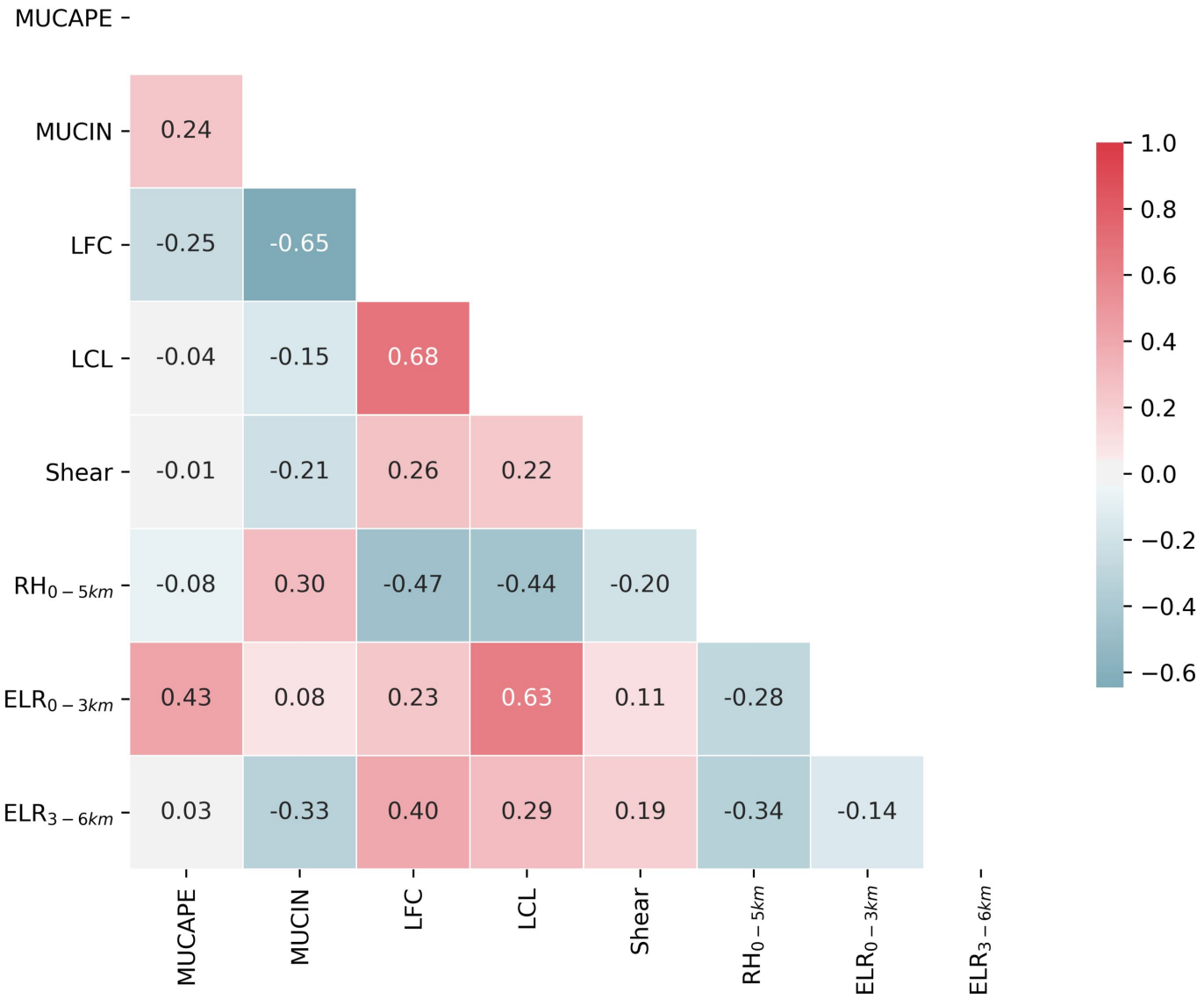
MUCAPE
MUCIN
LFC
LCL
Shear
RH_{0-5km}
ELR_{0-3km}
ELR_{3-6km}
0.24
-0.25 -0.65
-0.04 -0.15 0.68
-0.01 -0.21 0.26 0.22
-0.08 0.30 -0.47 -0.44 -0.20
0.43 0.08 0.23 0.63 0.11 -0.28
0.03 -0.33 0.40 0.29 0.19 -0.34 -0.14
1.0
0.8
0.6
0.4
0.2
0.0
−0.2
−0.4
−0.6

Figure 9.

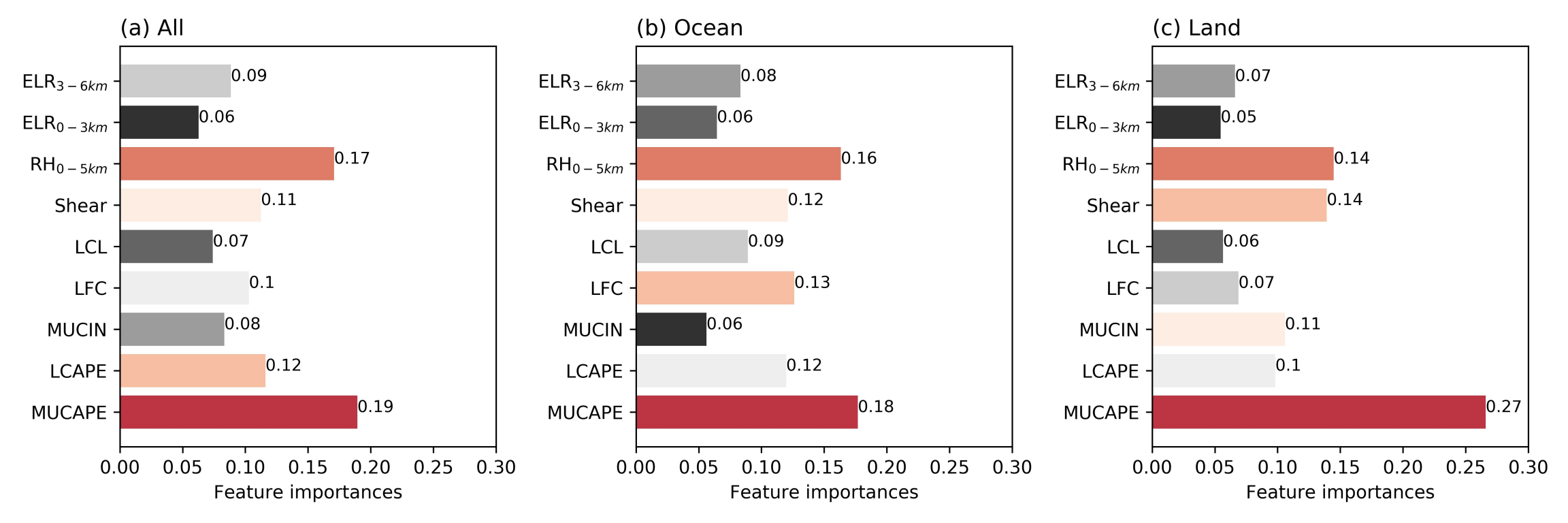
(a) All
ELR_{3-6km}
ELR_{0-3km}
RH_{0-5km}
Shear
LCL
LFC
MUCIN
LCAPE
MUCAPE
0.09
0.06
0.17
0.11
0.07
0.1
0.08
0.12
0.19
0.00 0.05 0.10 0.15 0.20 0.25 0.30
Feature importances
(b) Ocean
ELR_{3-6km}
ELR_{0-3km}
RH_{0-5km}
Shear
LCL
LFC
MUCIN
LCAPE
MUCAPE
0.08
0.06
0.16
0.12
0.09
0.13
0.06
0.12
0.18
0.00 0.05 0.10 0.15 0.20 0.25 0.30
Feature importances
(c) Land
ELR_{3-6km}
ELR_{0-3km}
RH_{0-5km}
Shear
LCL
LFC
MUCIN
LCAPE
MUCAPE
0.07
0.05
0.14
0.14
0.06
0.07
0.11
0.1
0.27
0.00 0.05 0.10 0.15 0.20 0.25 0.30
Feature importances